Lukas Kinner BSc

Inkjet Printed Metal Grid-Based ITO-free Electrodes for Organic Light Emitting Diodes

MASTER'S THESIS

to achieve the university degree of

Diplom-Ingenieur

Master's degree programme: Technical Physics

submitted to

Graz University of Technology

Supervisor

Ao.Univ.-Prof. Dipl.-Ing. Dr. techn. Emil J.W. List-Kratochvil

in cooperation with the
NanoTecCenter Weiz Forschungsgesellschaft mbH

Graz, October 2015

I Acknowledgement

From the beginning of my studies the day on which I would hand in my diploma thesis felt so far away, I never thought that it would come. Now as this thesis ends it is time to thank all the people who made this possible.

First I want to thank my supervisor Emil J.W. List-Kratochvil who brought me in contact with organic semiconductors and aroused my curiosity in OLEDs. Furthermore he supported my work from the first day and gave me the opportunity to work in an outstanding team, for which I am grateful.

A big “thank you” goes to Sebastian Nau. He guided me through this work as if it was his own. In experimental lean periods he gave me the necessary impulses to go on. Besides experimental details, he taught me what really matters in physics (or life as physicist? ;)). With his gentle but still professional manner he became more a friend than a supervisor to me.

Florian “the Mountain man” Kolb, took all the AFM pictures for this thesis. Although always in a hurry he always lent me his helping hand in the laboratory and cheered me up if necessary. Thanks a lot for that!

Manual Auer-Berger thank you for the basic introduction in OLED processing and for the “painful” guidance in cutting glass.

For this thesis a lot of inkjet printed metal grids were needed for my experiments. All this studies would have been impossible without Karl Popovic and Alex Wheeldon. No matter how full their timetable was, they always managed to supply me with sufficient grids.

I also want to mention the enlightening and helpful discussions with Stefan Sax about OLEDs, especially because I learned more about fishing then OLEDs. Further I want to thank you Stefan for providing me with the professional drawings of the embedding process and an OLED stack itself.

Without Gerburg Schider, I would lack of SEM images of silver nano wires, so thank you Gerburg.

Further I want to thank the whole team of the NanoTecCenter Weiz. The whole administration division, who were always patient with never ending requests about company processes. Last but not least: Thanks to all the people who were responsible for the labs, which made my experimental work much easier and to my colleges, who were always helpful. Thank You!

For the last 9 months I haven’t been only at the NTC-Weiz. In theory, I spent more of my time at home with my girlfriend Lena. As I said in theory, the truth is that I woke up went to Weiz and came home late. I want to thank you Lena that you supported me during this tough time. You never let me down nor complained although it was a stressful time. Thank You!

I wouldn’t be here writing this thesis without my family. My mother who was at home to give me a wonderful childhood, my father for giving me his fascination for nature and its wonders, thank you my parents.

I also want to thank my sisters and my brother for inspiring me to study and get an academic degree. Further that you always took care about your “small” brother.

Thank You!

II Abstract

This diploma thesis focuses on the investigation of transparent conductive electrodes for organic light emitting diodes (OLEDs) in order to replace the nowadays most commonly used indium tin oxide (ITO) electrode.[1] Such a novel setup is to be benchmarked against ITO by two key parameters, namely its transparency and its conductivity.[2] Furthermore, the raw material costs as well as processing costs have to be taken into account. Flexibility of the electrode material is also an important factor to consider, as future lighting applications should be applicable on curved shapes and bendable substrates.

In this context, inkjet printed silver electrodes are investigated. In order to reduce coverage and thus shadowing during light out coupling, honeycomb structures are chosen.[3] It is demonstrated that already at high coverage values (around 25%), the transmission in the optical wavelength range is comparable or better than conventional ITO.

In a first step, the functional layers of an OLED are deposited straightforwardly onto these grids. Highly conducive PEDOT:PSS is used to minimize voltage drop towards the center of a single honeycomb. To overcome the typically obtained feature heights as well as rough surfaces, a novel, commercially available high-viscosity and high-conductive PEDOT:PSS formulation was used. Although the IV-characteristics of these devices reveal significant parasitic shunt currents, they already show comparable performance values to ITO electrodes.

To reduce remaining shunt pathways through the device, a planarization/embedding process is applied in a second step.[4] This process is demonstrated for the first time for OLEDs and inkjet printed silver electrodes. The new embedded OLED configuration show significantly reduced shunt current compared the previous overcoated devices. Due to this optimized electrode structure, efficiencies of up to 9.4 cd/A and luminance maxima of 47000 cd/A were found for selected grid geometries. This represents an increase of 250% in efficiency compared to ITO.

Besides silver, also copper inks are evaluated with respect to their performance in OLEDs. Here, different sintering methods (formic acid sintering and laser sintering) are applied. For both processes, reasonably working OLEDs were fabricated showing that also copper grids can be used as transparent conductive electrodes. The efficiencies/luminance values of ITO based OLEDs are not fully reached, however the results can be considered as highly promising for future developments.

III Kurzfassung

Diese Diplomarbeit beschäftigt sich mit der Entwicklung und Untersuchung von transparenten, leitfähigen Elektroden für organische Leuchtdioden (OLEDs), um die heutzutage typischerweise verwendete Indium-Zinnoxid Elektrode zu ersetzen. Eine solche neuartige Elektrode wird an verschiedenen Parametern, beispielsweise deren Transparenz und Leitfähigkeit, qualifiziert. Weiters sind auch die Kosten für das Rohmaterial und die Prozessierung wichtige Punkte. Für spezielle Anwendungen, wie etwa flexible oder gekrümmte Beleuchtungsmittel, wird zusätzlich auch die mechanische Verformbarkeit der Elektrode gefordert.

In diesem Zusammenhang werde mittels der Tintenstrahldruck Technik hergestellte Gitterstrukturen aus Silber untersucht. Um die flächige Bedeckung und die daraus resultierende Abschattung des Lichts bei der Emission zu minimieren wählte man als Gitterstruktur eine Bienenwabenform. Es wird gezeigt, dass ab einer Bedeckung von etwa 25%, die Transmission im sichtbaren Wellenlängenbereich, die Transmission von ITO erreicht oder übersteigt.

Auf solchen Strukturen werden in weiterer Folge OLEDs prozessiert. Im ersten Schritt wird der OLED-Schichtaufbau direkt auf das Gitter aufgebracht. Dabei wird hoch leitfähiges PEDOT:PSS verwendet, um den Spannungsabfall zum Zentrum der einzelnen Hexagonstrukturen so gering wie möglich zu halten. Tintenstrahl gedruckte Strukturen sind in der Regel relativ hoch und rau. Um diese ausreichend zu bedecken wird eine neueartige, kommerziell erhältliche hoch viskose und hoch leitende PEDOT:PSS-Formulierung verwendet. Obwohl die IV-Charakteristiken dieser Bauteile hohe Leckströme aufwiesen, kann bereits mit OLEDs basierend auf einem solchen Elektrodensystem die Effizenz von ITO-basierenden OLEDs reproduziert werden.

Um solche ungewünschten parasitären Leckströme durch das Bauteil zu verkleinern, werden die Gitter in einem zweiten Schritt eingebettet und dadurch planarisiert. Ein solcher Prozess wird hier erstmals für OLEDs und tintenstrahl-gedruckte Silberwaben präsentiert. Verglichen mit den ersten Bauteilserien, zeigen die eingebetteten Bauteile deutlich reduzierte Leckströme. Dank dieser optimierten Bauweise können Effizienzen bis 9.4 cd/A und Lumineszenzen bis 47000 cd/m^2 an ausgewählten Gitterstrukturen erreicht werden. Dies entspricht einer Steigerung der Effizienz um 250% im Vergleich zu konventionellen ITO-basierenden OLEDs.

Neben Silbertinte werden auch Kupfertinten in Bezug auf ihre Tauglichkeit als Elektrode in OLEDs erforscht. Dabei kommen verschiedene Sinterprozesse (Ameisensäure- und Lasersintern) zum Einsatz. Mit beiden Prozessen werden erfolgreich funktionstüchtige OLEDs auf den Gitterstrukturen demonstriert. Die Effizienz/Lumineszenz von ITO-basierenden OLEDs werden hier nicht erreicht, allerdings können die Ergebnisse als sehr vielversprechend, für künftige Entwicklungen auf diesem Gebiet eingestuft werden.

IV Table of contents

V List of abbreviations

ITO	Indium Tin Oxide
PEDOT	Poly(3,4-ethylenedioxytiophene)
PSS	Polysterenesulfunate
OLED	Organic light emitting diode
PLED	Polymer light emitting diode
AgNW	Silver nano wires
IV-characteristics	Voltage-current characteristics
Alq3	Aluminium-tris(8-hydroxychinolin)
NPB	N,N'-Di(1-naphthyl)-N,N'-diphenyl-(1,1'-biphenyl)-4,4'-diamine
HIL	Hole injection layer
LEP	Light emitting polymer
CP	Copolymer

1 Introduction and motivation

Organic light emitting diodes (OLEDs) are getting more and more a part of our everyday live.[5] Many providers of consumer electronics feature OLEDs in displays and lighting applications.[6] OLEDs comprise many positive features, e.g. their potential low production costs, light weight and the possibility of processing them from solution at low temperatures, are few to mention.[7] Furthermore, they are energy efficient in operation and achieve high contrast ratios. The opportunity to process OLEDs on virtually every substrate, even flexible ones, offers further possibilities for lighting applications and new design options.[8] Inkjet printing offers the possibility to include this features and to process solution processed OLEDs on various substrates cheap and fast.[9] Summing up, OLEDs offer promising features for future lighting applications.

As a matter of fact it requires at least one (semi-) transparent electrode to allow out coupling of generated light. Until now, in most commercial applications indium tin oxide (ITO) is used as a transparent electrode due to its positive properties, including a low sheet resistance (around 6 Ω/□) in thin films combined with a high transmission of about 85% over the whole visible spectrum. [10] However, ITO films are rigid and brittle.[11] Further on, an energy consuming high vacuum sputtering process is needed to deposit the films. This is one of the reasons that OLEDs are still too expensive for lighting applications. Therefor OLEDs are only applied in niche lighting applications so far. The scope of this work is to investigate an alternative transparent conductive electrode (TCE) to ITO. To satisfy the demands on easy and cheap process ability inkjet printed metal grids were used as TCEs, applied in OLEDs and evaluated by the OLED performance.

Chapter 2 comprises the theoretical background of organic semiconductors.

In chapter 3 the basic working principle of an OLED is explained. Details of light generation and basic material topics are discussed. Chapter 4 comprises all experimental details. All applied processes and measurments techniques are explained. Chapter 5 shows a multilayer light emitting diode (PLED) processed on ITO, which was further used as a reference device. Chapter 6 presents OLEDs using a metal grid layout as an alternative to ITO. The grids have been fabricated by a high volume industrial scale print head. This first set of grids was made of Ag nano particle ink and were overcoated with PEDOT:PSS. These first grids already showed a comparable performance to ITO.

In a second step, the same grid structures were embedded in an UV-curable hybrid polymer layer, in order to planarize the electrode and further increase the efficiency.

Chapter 7 deals with the properties of two different copper inks for inkjet printing. These inks were used to print the same grid structures as with silver ink. To compare the performance of these two inks the same experiments were carried out as before. Finally in chapter 8 an alternative approach is shown. This chapter deals with silver nanowires as transparent conductive electrodes. Nanowires can be seen as highly disordered micro grids. Applied in thin films, nanowires could be used as transparent electrodes. Further details are presented in this chapter. Chapter 9 presents a conclusion of the performed experiments.

2 Organic semiconductors

This chapter deals with the basics of organic semiconductors. A short explanation on carbon atoms and its binding ability to form molecules and polymers is given. Further the details of organic conduction and light generation are discussed.

2.1 Carbon bonds

Organic by common sense means a compound of carbon atoms. The basis of organic bonds is hybridization of atomic orbitals.[12] Carbon has 5 atomic orbitals. Its electron configuration is $1s^2 2s^2 2p_x 2p_y$. The s orbital has a spherical shape and the p orbital a dumbbell shape. The $2p_z$ orbital remains empty in the neutral atom and only the 4 outer electrons in the $2s^2$, $2p_x$ and $2p_y$ orbitals contribute to chemical bonding. Hybridization means, that these orbitals can form an intermediate orbital state with an intermediate energy level to form a chemical bond. Hybridization is favourable as it lowers the overall energy of the orbitals. The three types of hybridization will be explained in the following.

Figure 1 shows the ethene molecule as an example. The left sketch shows the atomic sp^2 and s orbitals which overlap to covalent bonds. Figure 1 (right) shows the molecular bonds, π bonds for the overlap of the p orbitals and σ bonds for the overlapping sp^2 orbitals.

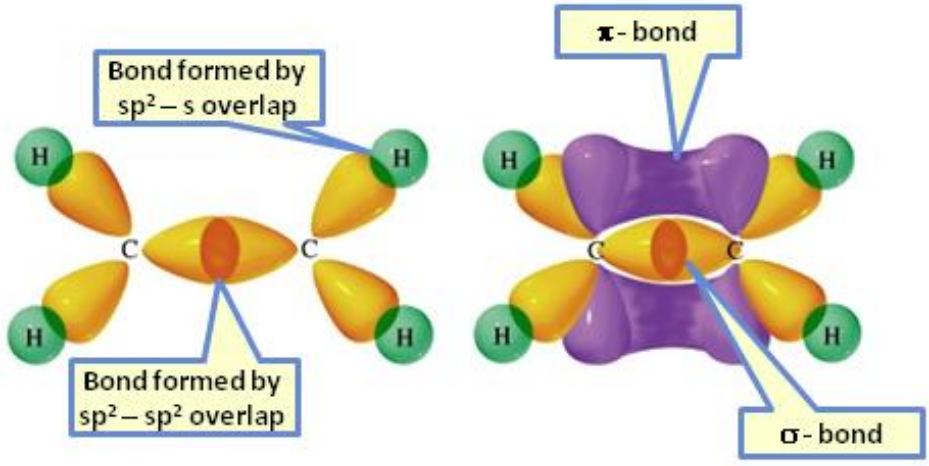

Figure 1: Ethene molecule with its bonds taken from [13]. Left: 2 carbon and 4 hydrogen atoms form a molecule by hybridization. The yellow dumbbell shaped orbitals represent sp^2-hybridized orbitals. Right: The formation of all bonds by overlap are shown. Two sp^2 orbitals form a σ bond, overlap of two p orbitals form a π bond.

sp^3 hybridization

Two s orbitals can hybridize with two p orbitals. This gives 4 energetic identically sp^3 orbitals which are lower in energy than the sum of the ground state orbitals. Caused by electrostatic forces those 4 orbitals try to be as far apart as possible. They form an imaginary tetraeder around one carbon atom. Four hybridized orbitals can overlap with those of a neighbouring carbon atom, leading to strong covalent bonds. sp^3 orbitals form 3 dimensional structures. Figure 2 shows the energetic relationship between hybridized and ground state orbitals. Overlap of sp^3 orbitals form σ bonds as shown in Figure 2.

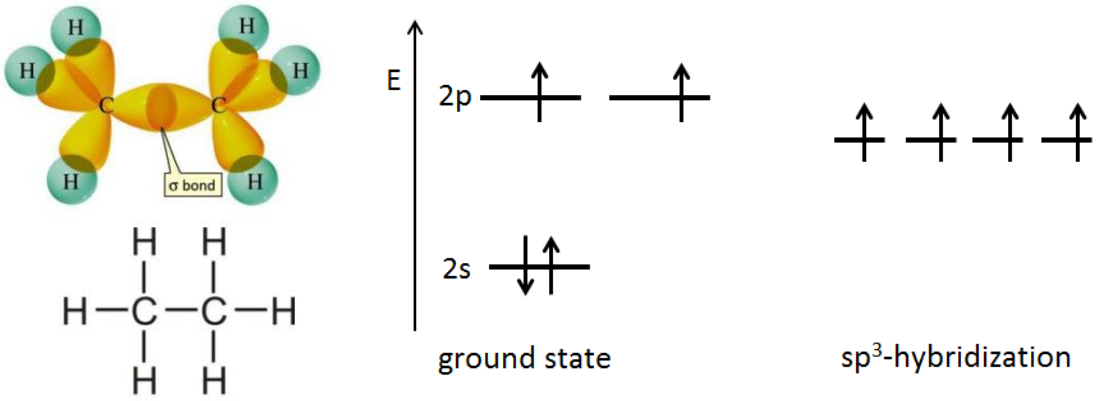

Figure 2: Schematic representation of sp^3 hybridization. Right: 2s and 2p orbitals hybridize to form 4 energetically identically orbitals which are lower in energy then the ground state. Left: Ethane molecule with according bonds taken from [14].

sp^2 hybridization

This type of hybridization consists of two s orbitals but only one p orbital. 3 hybridized sp^2 orbitals spread out in one plane and the remaining p orbital stands out of plane. The not hybridized p-orbitals overlap additionally to the sp^2 hybridized orbitals. This leads to a double bond formed by 2 energetically different orbitals. This energy discrepancy in orbitals forms the prerequisite requirements for organic semiconductors. Figure 3 displays the energies of the orbitals, the three lower lying orbitals have lower energy then the sp^3 orbitals in Figure 2. The overlap of sp hybridized orbitals is denoted as σ bonds and the overlap of p orbitals as π bonds. π bonds are found in all organic semiconductors.

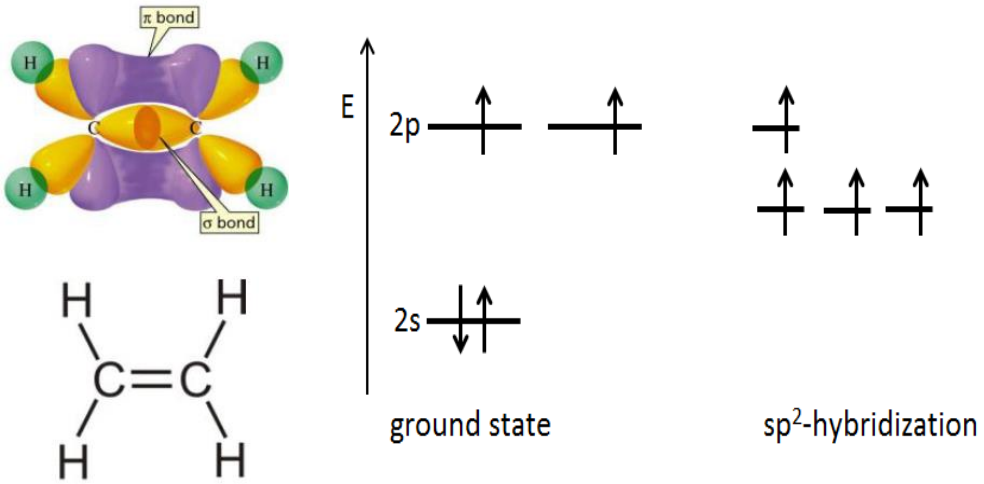

Figure 3: Right: Schematic representation of sp^2 hybridization, 3 energetically identical and one energetically higher lying orbital are formed. Left: Ethene molecule with according bonds, taken from [14].

sp^1 hybridization

In this type of hybridization, one s orbital hybridizes with one p orbital. The remaining two p orbitals build-up 2 more bonds, which lead to a triple bond. Triple bonds form one-dimensional chains. Figure 4 displays again the energy relations, the 2 lower lying orbitals are energetically even below the sp^2 orbitals. This leads to a high reaction potential of triple bonds.

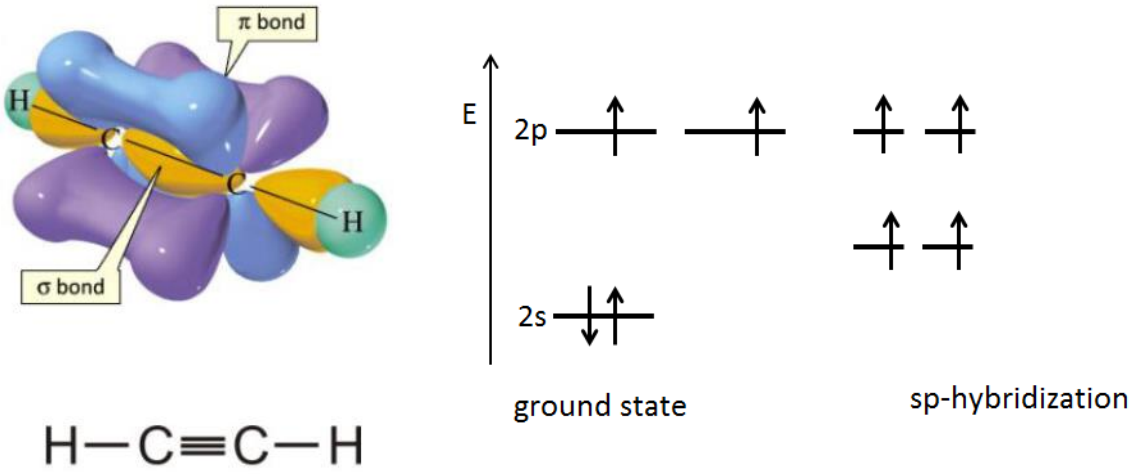

Figure 4: Schematic representation of sp hybridization. Right: One s and one p orbital hybridize to two sp orbitals, which are lower in energy then other hybrid orbitals of carbon molecules. The two remaining 2p orbitals are energitcally higher. Right: Ethyne molecule with according bonds taken from [14].

2.2 Conjugation and molecular orbitals

According to molecular orbital theory, molecular orbitals are described as a linear combination of atomic orbitals. [15] This is equivalent to the description of overlapping hybridized carbon orbitals and the resulting chemical bonds (σ and π). π orbitals are formed by the p_z orbitals of the carbon atom. p_z orbitals stand out of the imaginary plane formed by σ bonds and the carbon atoms. Therefore π electrons (electrons in π orbitals) are not as strong bound to one atom as the electrons in the σ bonds formed by sp^2 overlap.[16][17] The alternation of single and double bonds in organic molecules is called conjugation. Conjugation leads to a delocalisation of the π electrons over the molecule, polymer. [18] Conjugation causes the semiconducting properties of organic molecules. Concerning electron energy π orbitals form the highest occupied- (HOMO (π)) and lowest unoccupied molecular orbital (LUMO (π^*)). π^* denotes the antibonding orbitals. The antibonding π^* orbitals are higher in energy than the π orbitals causing a band gap between HOMO and LUMO.[19]

HOMO and LUMO can be compared to the valence and the conduction band, of an inorganic semiconductor.

However, the conduction properties of an inorganic and organic semiconductor differ.

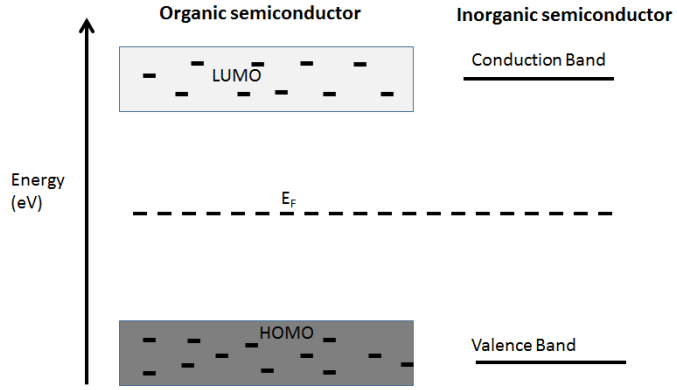

Figure 5: Schematic representation of energy levels (bands) in an organic semiconductor (left) and an inorganic semiconductor (right); on the left is the energy scale; E_F denotes the Fermi energy.

Figure 5 compares an organic (left) and an inorganic (right) semiconductor. The broad variation of energy levels in the HOMO and the LUMO is caused by disorder, vacancies and inhomogenities. These effects are more prominent in organic materials then in crystallite solids. The various possible energy levels are represented by the short black lines. Consequently in an organic semiconductor the charge transport is hopping dominated which was originally described by the Marcus theory. [20] This leads to very low charge carrier mobilities compared to an inorganic semiconductor.

HOMO and LUMO are filled with charge carriers according to a Gaussian distribution. Figure 5 (right) shows an inorganic semiconductor. Due to its crystal structure the inorganic semiconductor has sharp defined valence and conduction bands. The difference in energy distribution on microscopic scale leads to different properties in lighting applications. Inorganic LEDs have sharp-defined emission spectra, while OLEDs have broad spectra.

Conductivity is the product of mobility, number of charge carriers and elemental charge, as shown in Equation 1. Therefor conductivity can be increased either by increasing the number of charge carriers or by increasing the mobility. Hopping is a thermally driven process, therefor organic semiconductors conduct better at higher temperatures. The number of charge carriers can be increased by doping (e.g Iodine or Nitrogen in Polyacethylene) in the organic compound. [21]

$$\sigma = n * q * \mu$$

Equation 1: σ…conductivity; n...mobility; q...elemental charge; μ...Mobility

2.2.1 Polarons

Charge carrier, which are moving through an organic solid are attracting the positively charged cores atomic cores and reject negative electron clouds or vice versa.[22] This polarisation cloud moves with the particle through the organic solid and increases the effective mass of the charge carrier. Due to the increased effective mass the charge carriers loose total energy and occupy energetic lower lying intra band states. One can think of a charge carrier deaccelerated by the surrounding charges. The resulting quasi particle is called polaron. Figure 6 shows the energy shift of polarons. Further the different types of polarons are displayed. A positive polaron can be seen as a missing electron (hole) in the HOMO, while a negative polaron can be seen as an additional electron in the LUMO. The term bipolaron describes a combination of two positive or negative polarons.

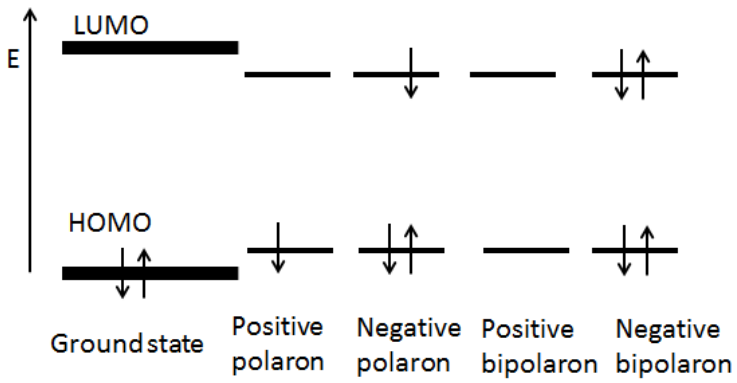

Figure 6: Energetic relations of various polarons are shown. The term positive polaron describes a missing electron in the HOMO (hole), negative polaron describes an additional electron in the LUMO, the term bipolaron refers to 2 polarons.

2.2.2 Excitons

An exciton is a bound pair of a neagitve and a positive polaron. [23] Depending on the distance between the 2 charge carriers, one can distinguish between Frenkel and Mott Wanier excitons. Frenkel excitons are localised on one molecule and feature a distance in the range of 1 nm. Mott Wanier excitons are spread further over the solid. Only Frenkel excitons are found in organic semiconductors due to strong inhomogeneities compared to inorganic crystals.[24]

An exciton is a neutral quasi particle hence it can carry energy without carrying charge, nevertheless the bounded charge carriers have a spin. Hence, an exciton does not have a netto charge but a netto spin. Due to the linear combination of up and down spin, singlet and triplet excitons can form. Equation 2 describes the wave function of a singlet exciton with total spin zero while Equation 3 describes the possible wave functions of a triplet exciton with total spin one. Due to the 3 possible triplet and one possible singlet formation of excitons, excitons obey a 25% to 75% ratio in OLEDs. [25]

$$\Psi_s = \frac{1}{\sqrt{2}}(|\uparrow\downarrow\rangle - |\uparrow\downarrow\rangle)$$

Equation 2 : Wave equation for a singlet exciton.

$$\Psi_t = |\downarrow\downarrow\rangle$$
$$\Psi_t = |\uparrow\uparrow\rangle$$
$$\Psi_t = \frac{1}{\sqrt{2}}(|\uparrow\downarrow\rangle + |\uparrow\downarrow\rangle)$$

Equation 3: Wave equations for triplet excitons.

2.2.3 Optical processes in organic semiconductors

Figure 7 shows the schematic representation of the ground state and the first excited state of a 2 atomic molecule. All considerations can be applied for larger molecules with more atoms because of the Born Oppenheimer approximation. According to the Born-Oppenheimer approximation the wave function of a molecule can be described as product of its electronic and nuclear wave functions. [26]
In Figure 7 the ground state of the molecule is stated with S_0. In a two atomic molecule the ground state wavefunction can be calculated by solving the Schrödinger equation. The potential term in the equation can be estimated with a parabolic form.

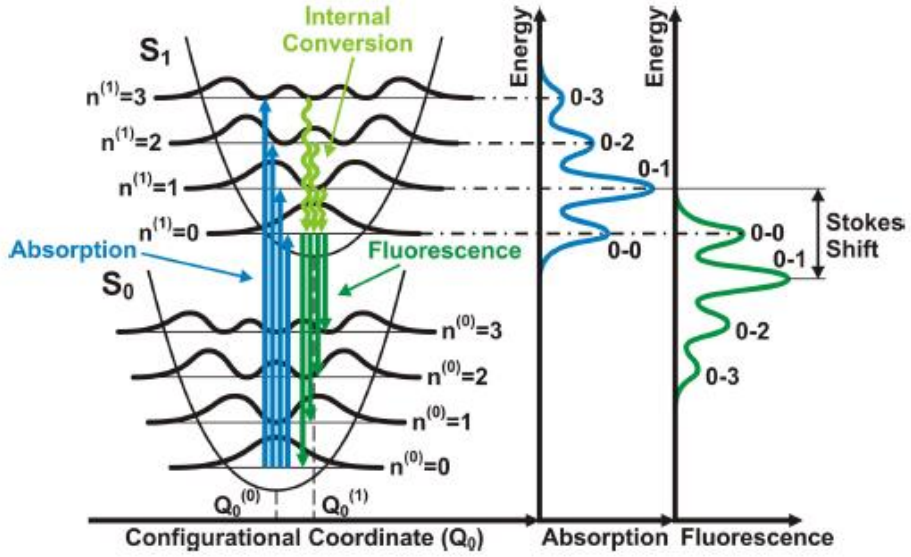

Figure 7: Two electronic states with various vibronic states, S_0 labels the singlet ground state while S_1 is the singlet excited state. The straight lines stand for stimulation and decay under radiation while the wiggled lines mark radiationless decay. Taken from [27].

The index n in Figure 7 is called quantum number and denotes to the increasing vibrational modes of the molecule.[28] S_1 is the first excited singlet state of the molecule with according vibrational modes. A transition can occur if a photon with sufficient energy is absorbed by the molecule (blue arrows in Figure 7). According to the Frank Condon principle the probability of a transition is higher if the wave functions in the S_0 and S_1 state have the same probability density.[29-31]
The offset in configurational coordinates of the 2 potential wells is further noticeable. This is caused by the reason that transitions between HOMO-LUMO always change the bond lengths of the molecule. As a consequence the potential energy curves for ground and excited state show a displacement.
Vibronic relaxations take place in about 10^{-18} s and electronic transitions take place in 10^{-15} s.[32] This results in the fact that internal conversion to the lowest lying vibrational mode in the excited

electron state happens before an electronic relaxation takes place. Internal conversion for vibronic states refers to thermalisation. From this fact derives usually absorption spectra are mirrored emission spectra. This phenomena is called Stokes shift and shown in Figure 7.

Jablonski diagram

The Jablonski diagram shows all possible light induced molecule transitions. In a jablonski diagram the excited states and transition rates are drawn.[33] Starting with a molecule in singlet ground state (S_0) absorption of a photon excites the molecule to an excited vibrational state. The dashed lines in Figure 8 symbolise vibrational modes. From the vibrational mode the molecule relaxes to the first excited state S_1 in approximately 10^{-18} s. The molecule remains in the S_1 state for approximately 10^{-15} s. Fluorescence (k_{FL}), the radiative recombination of an electron hole pair, can only take place for singlet excitons as the total spin needs to be conserved. k_{nr} denotes the non-radiative decay rate from the S_1 to the S_0 state. If the molecule is in the excited state (S_1) it can undergo an inter system crossing (k_{ISC}) to a triplet state (T_1). The radiative recombination of triplet excitons is quantum mechanically forbidden due to spin-orbit coupling. Nevertheless quantum mechanically forbidden means that this transitions are rare but can happen after a certain period of time. (Denoted as lifetime of the excited state.) The lifetimes of the T_1 states are in the range of micro seconds up to milliseconds and in rare cases up to hours for phosphorescence (k_{ph}). Phosophorence is the radiative decay from the T_1 to the S_0 state and $k_{nr\ ph}$ denotes the non-radiative rate from T_1 to S_0. To weaken the spin orbit coupling and make the transition possible for a triplet exciton (k_{PH}) heavy elements (e.g. Ir) can be added to the compound.

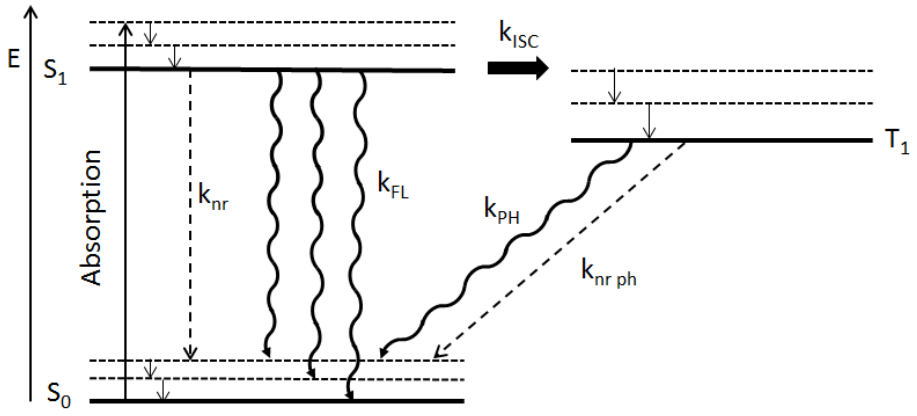

Figure 8: Jablonski diagram of an arbitrary organic semiconductor where S_0 and S_1 denote the singlet ground and excited state. T_1 represents the triplet state. The dashed lines stand for vibronic states. k_{nr} denotes the non-radiative recombination rate of an exciton. k_{fl} is the rate for fluorescent recombined excitons. k_{isc} describes the rate of inter system crossing. k_{PH} is the rate of phosphoresecent recombined excitons. The rate of non-radiative decay of phosphorescent transitions is denoted by $k_{nr\ ph}$.

3 Working principle of OLEDs

The following chapters explain the basic working principles of an OLED. Further the different layers and the according materials are explained. As organic materials are prone to degradation, in oxygen and humid atmosphere, degradation effects are also explained briefly.

Electroluminescence

The basic set up of an OLED includes at least one organic semiconductor between two electrodes. If an electric field is applied charge carrier can be injected into the organic semiconductor. This electrons and holes recombine under the radiation of light. This principle is called electroluminescence. [34] Figure 9 shows the schematic set up of the OLEDs presented in this thesis. At the bottom is usually a transparent substrate. This can be glass or a flexible, transparent material. In state of the art OLEDs a structured layer of ITO is sputtered on this substrate. On top of the ITO layer follows a layer of PEDOT:PSS for smoothening and hole-injection reasons.

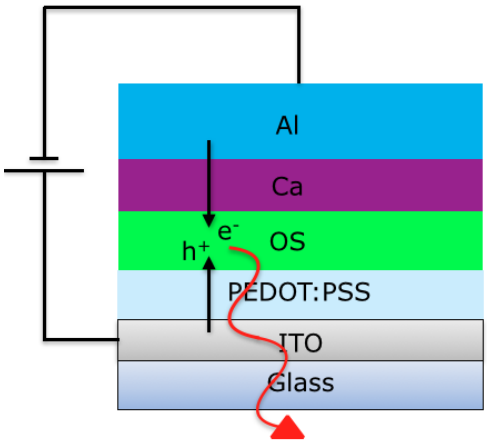

Figure 9: Standard OLED/PLED device stack; from bottom to top: transparent substrate; structured ITO layer; PEDOT:PSS layer; light emitting layer; Calcium layer; Aluminium layer; the black arrows represent holes respectively electrons which are injected; the red wave line represents the generated photon.

The core of the OLED is the light emitting layer, which consists of an organic semiconductor. Here the injected electrons and holes form excitons and recombine under the generation of light. To achieve a low injection barrier for electrons at the interface, a thin layer of a low work function material (e.g. Ca, Ba, LiF) is evaporated on the stack of organic layers.[35] More details are explained in 3.2 metal-organic interfaces. To avoid degradation from Oxygen and humidity and to get a better conductivity the final layer consists of Aluminium.

Metal-Organic Interfaces

As shown above, an OLED device consists of several layers of organic and inorganic materials. As charge carrier injection is crucial for electroluminescence a closer look on the interfaces is given. Due to different Fermi energiey of the participating materials, energy barriers at the interfaces are formed. Starting point of the discussion are metal-organic interfaces, which are the main interfaces for charge carrier injection from the metal electrode into the organic semiconductor. These barriers should be kept low to achieve increase the number of injected charge carriers. The basic considerations for interfaces are band bending and energy level alignment. If separated in spcace metal and organic layer share a common vacuum level (Figure 10 left). Figure 10 additionally shows the work function (ϕ_m) of the metal, the Fermi energies of the materials (E_f), the work function of the organic layer (ϕ_{org}), the electron affinty (A), the ionisaiton potential (I) and the LUMO and HOMO. If brought into direct physical contact, a dipole layer is formed at the interface (Figure 10 right). Electrons have a finite space distribution probability outside the bulk. This electrons attract positive charges in the organic layer and a dipole is formed. This dipole layer leads to a change in the form of the barrier between the materials as shown on the right side of Figure 10. The shift of energy can increase or decrease, depending on the work function of the metal and the organic semiconductor.

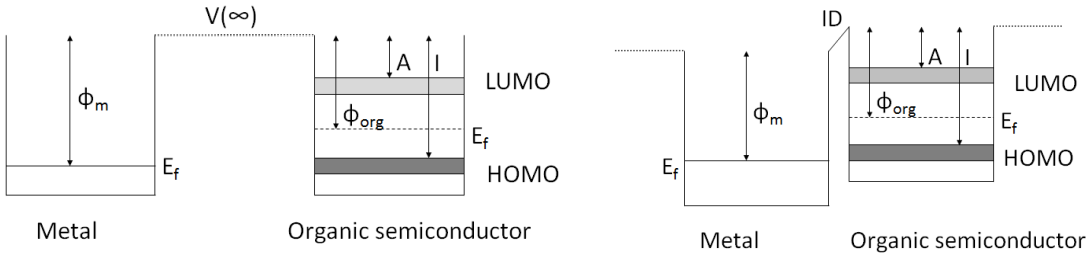

Figure 10: Left: Metal and organic semiconductor are far apart and share a common vacuum level. Right: Metal and organic semiconductor form an interface and a dipole layer. Further shown are the metal work function (ϕ_m), the Fermi energies of the materials (E_f), the work function of the organic layer (ϕ_{org}), the electron affinity (A), the ionisation potential (I), LUMO and HOMO.

Additionally to the ID (interface dipole) barrier, band bending of the HOMO and the LUMO take place (not in figure). The fermi levels of the materials which are brought into contact have usually different work functions. In Figure 10 E_f of the metal is lower as for the organic semiconductor. Electrons move to the metal side, creating a built in potential. This potential leads to a bended E_f at the interface. Band bending can only occur if sufficient mobile charge carriers are present.[36-37]

Organic-Organic Interfaces

Besides metal-organic interfaces OLEDs also feature organic-organic interafaces. Dipole layer like in the previous described metal-organic interfaces also occur if two organic materials are brought in contact. The vacuum level shift is not as high as in metal-organic interlayers and hence do not lead to strong band bandings. Band bending effects are generally small at organic-organic interfaces.[37]

3.1 Light generation

Figure 11 shows the active layer, the PEDOT:PSS cathode and the Calcium anode in the so called flat band regime. The flat band regime represents the OLED under a small enough forward bias to flatten the LUMO and the HOMO. Further, in figure shows the work function of PEDOT:PSS (5.0 eV) [38] and Ca (2.9 eV) [38], the electron affinity (E_a), the band gap (B_g), the ionisation potential (I_p) and the vacuum level.

Figure 11 (right) shows the same relations under an applied forward bias. Caused by the forward bias an increase of the potential at the cathode side and a subsequent alignment of the energy levels in the device is observed. The work functions of the different materials remain constant. The lowest unoccupied molecular (LUMO) and the highest occupied molecular orbital (HOMO) also align according to this circumstances.

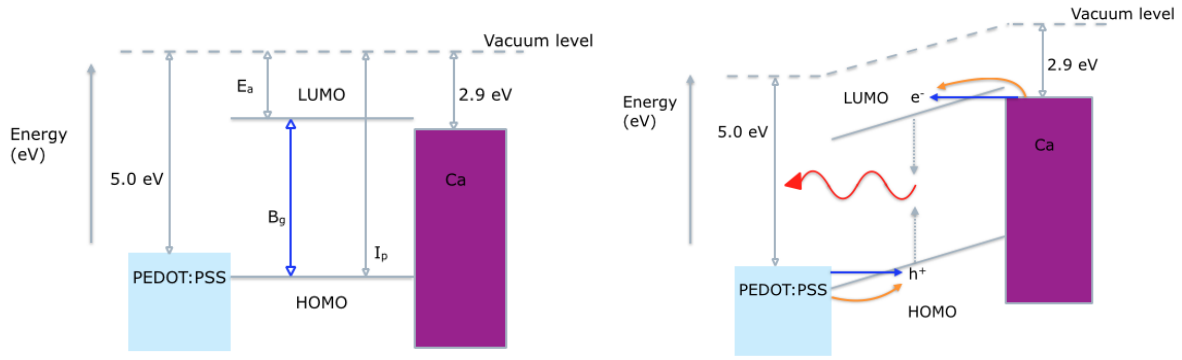

Figure 11: Left: Flat band regime of an OLED device, E_a electron affinity, B_g band gap, I_p ionisation potential are shown. Further the energy relations are shown of PEDOT:PSS anode, active layer and cathode. Right: OLED under forward bias, the blue arrows symbolize charge carrier injection via tunnelling, yellow arrows denote injection due to thermal emission. e^- h^+ denote electrons and holes, the red wave line symbolizes emitted light.

This leads to the formation of triangular shaped energy levels (Figure 11 right, right top and left bottom). Through this triangular shaped energy barrier electrons and respectively holes can be injected via tunnelling (blue arrows).

Injected holes and electrons move along the active layer under the influence of the electric field, until Coulomb interactions become dominant and form an exciton[32]. From the exciton state the electron and hole can recombine under the emission of light. The wavelength of the light is determined by the size of the bandgap.

$$J = \frac{A^* T^2}{\phi}\left(\frac{qE}{kTm * \kappa}\right)^2 exp\left(-\frac{2\kappa\phi^{2/3}}{3qE}\right)$$

Equation 4: Fowler Nordheim equation: J…injection current; κ…shape parameter; m*…effective mass; h… Planck´s constant; E…applied electric field; k…Boltzmann constant; T…Temperature; ϕ…barrier potential; A…cross section area

The tunnel current is described by the Fowler Nordheim equation (Equation 4).[39] The current (J) is proportional to the applied electric field sqaured (E^2) and the barrier potential (ϕ), therefor increasing with applied voltages and lower potential barriers.

The orange arrows in Figure 11 symbolise the thermal injection into the active layer. Thermal injection is a far smaller contribution then tunnelling.

As mentioned previously, both mechanisms are only very rough approximations. The Richardson Dushman equation (Equation 5) describes thermionic electron emission from a metal into the vacuum where the electrons are allowed to propagate freely, whereas in a conjugated polymer the charge carrier are highly localized. The injection current (J) increases with temperature squared (T^2).

$$J = A_G T^2 e^{\frac{-W}{kT}}$$

Equation 5: Richardson Dushman equation with J…emission current; A_G…Richardson constant; T…temperature; W…work function of cathode material; k… Boltzman constant [40]

OLED characteristics

The characteristics of OLEDs can give information on figures of merit related to the device performance. The voltage-current characteristics gives information on the rectification of the device. To obtain a voltage-current characteristics a voltage sweep is performed on the device and the corresponding currents are measured. A material and layer dependent property is the luminescence onset voltage. For this thesis the luminance onset voltage is defined as voltage at 100 cd/m^2. An exponential increase in current density and luminance from the onset is desired. In backward bias the current should be low. If the cut-off current is high it is an indicator for shorts through the OLED layers. For the same reason the current in forward bias should be as low as possible until the onset

voltage. From the voltage-current-luminance characteristic the efficiency of the device can be calculated.

Photoluminescence quantum yield (PLQY)

With photoluminescence measurements information on the electronic and vibrational transitions in a molecule can be gathered. The photoluminescence quantum yield (ϕ, Equation 6) is described as the number of photons emitted, divided by number of photons absorbed and builds the basis for the electroluminescence quantum yield which is an efficiency parameter of an OLED.

$$\Phi_{PL} = \frac{\text{number of photons emitted}}{\text{number } of\ photons\ absorbed} = \frac{k_r}{k_r + k_{nr}}$$

Equation 6: ϕ_{PL}…PLQY; k_r denotes the rate of radiative decay, whilst k_{nr} represents the opposite, non-radiative decay.

Electroluminescence quantum yield

Equation 7 describes the quantum efficiency (η) of a PLED. η is basically defined as the number of charge carriers injected divided by the number of photons emitted by an electroluminescent device. Equation 7 shows further factors influencing η.

$$\eta = \Phi_{PL} * r_{st} * \gamma * X$$

Equation 7: η…Electroluminescence quantum yield; ϕ_{PL}…PLQY; r_{st}…singlet triplet ratio; γ…ratio of injected charge carriers and formed excitons; X…quenching factor

Besides radiative recombination, there are other ways for an excited state to release its energy, as described in detail in the Jablonski diagram.

r_{st} takes the singlet-triplet ratio into account. In contrast to ϕ_{PL}, r_{st} is the number of excitons which are able to recombine under radiation divided by the total number of excitons generated.

The number of excitons formed over the total number of charge carriers injected is described by the factor ɣ. To improve ɣ and therefor get a higher efficiency charge blocking layers can be placed between the electrodes and the organic layers. This helps to balance charge currents in the layers and get an increased efficiency.

X represents all factors which further decrease light out-coupling, for example self-absorption in the active layer, also interference and total reflection at interfaces. Further X also includes all types of quenching.

3.2 Functional layers of OLEDs and degradiation problems

State of the art OLEDs feature many functional layers. An increasing number of functional layers are added for different reasons in an OLED stack. Also different materials and methods for processing are applied in nowadays OLEDs. The following is a list of the basic principles, materials and processes for manufacturing an OLED.

Basically there are two different types of organic light emitting materials, small molecules and polymers which are further explained in detail.

Small molecules

Small molecules are molecules with a molecular weight lower then 800 g mol^{-1}. Small molecules can be thermally evaporated or spin coated to achieve thin films. The first electroluminescent device was built by Tang et al.[41] Therefor the aromatic diamine Tris(8-hydroyquinolinato)aluminium (Alq3) was used. It is shown in Figure 2. Alq3 is a widely used material in OLEDs. It can be applied via vacuum evaporation.

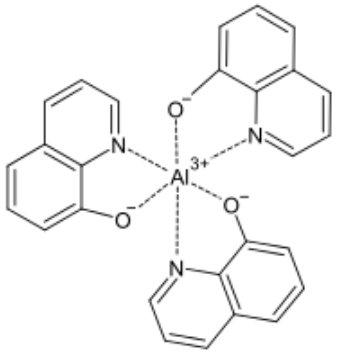

Figure 12: Chemical structure of Tris(8-hydroxyquinolinato)aluminium (Alq3), taken from Ref [42].

Polymers

Second commonly used type of organic compounds are polymers. The resulting devices are denoted as polymer light emitting diodes (PLEDs). [38] Polymers consist of many repeating units. Those repeating units are called monomers. A polymer can consist of 10^2 - 10^5 repeating monomers.[14] Polymers consisting of more then one type of monomer are called copolymers. Copolymers have different chemical groups on the polymer chain to tune desired properties, for example to enhance the conjugation, conductivity or chemical stability of the polymer Polymer thin films are mostly solution processed via spin coating of printing. The first polymer-based electroluminescent device was first demonstrated in poly(p-phenylene vinylene) (PPV) films.[34]

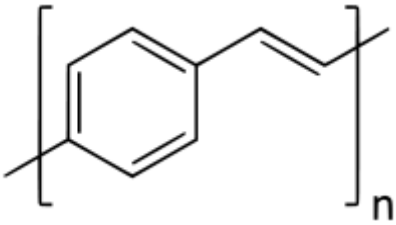

Figure 13: Chemical structure of Poly(p-phenylene vinylene), a semi conducting polymer showing electroluminescence taken from [34].

Hole injection layer (HIL)

As mentioned in previous chapters, additional layers can enhance the efficiency of OLEDs. The main steps of light generation (charge injection, conduction, recombination) demand different material properties. [34]. First to mention, because of their use in this thesis, are hole injection layers (HIL). As shown in Figure 11 between the PEDOT:PSS layer and the organic semiconductor there is a step in energy. To reduce this step height and hence allow for an increased charge carrier injection a HIL is introduced. It should have an intermediate HOMO between anode and light emitting layer (LEM). Further, a HIL should have hole blocking abilities to hinder holes from leaving the active layer without recombining.

PEDOT:PSS and its variations

Figure 14 shows the chemical structure of PEDOT (Poly(3,4-ethylenedioxythiophene)) and PSS (polystyrene sulfonate). PEDOT:PSS is a mixture of PEDOT and PSS. PEDOT:PSS is an electrical conducting polymer.[43] It is used in the previously mentioned devices as smoothening and hole injection layer. The layer thickness of PEDOT:PSS is controlled by the according process parameters. (e.g.: here spincoating parameters) Subsequently to layer deposition PEDOT:PSS needs to be thermally treated, to remove residual solvents. PEDOT is a conjugated polymer on thiophene basis, whereas PSS is an isolator. When mixed, PSS acts as dopant for PEDOT to achieve the electrical conductivity in thin films. PSS is acidic with a pH value of approximately 1.5-2.5. Depending on the physical demands of the PEDOT:PSS layer, various formulations of the solutions are available on the market.

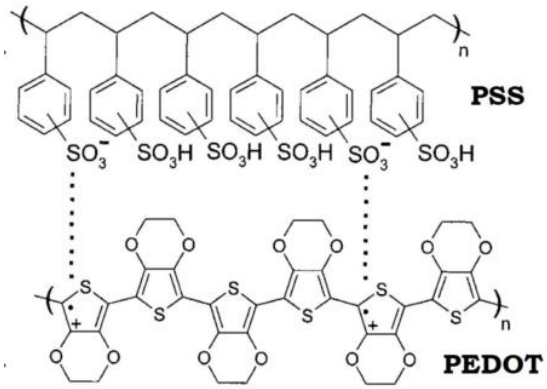

Figure 14: Chemical structure of poly(3,4-dioxythiphene) polysterene sulfonate taken from [44].

For the ITO reference samples in this thesis the well known formulation P VP Al4083 was used. This formulation has a PEDOT:PSS ratio of 1:6 per weight. Additionally the F CE formulation with no given ratio of PEDOT:PSS was used. F CE PEDOT is based on so called highly conductive PEDOT:PSS. Highly conductive PEDOT:PSS usually has a PEDOT:PSS ratio of 1:2.5. The lower mixing ratio causes higher doping and this higher conductivity of the layer. The F CE formulation is a special creation for overcoating inkjet printed lines. Hence it has a higher viscosity, 15-70 mPas compared to 5-12 mPas for the P VP Al4083 formulation.

3.2.1 Transparent conductive electrodes (TCE)

Transparent conductive oxides (TCOs)

The most common used transparent electrode in OLEDs and hence most prominent oxide is indium tin oxide (ITO). ITO features transparency of 85% in the opticle spectral range and relatively low sheet resistances (6 Ω□).[45] Tin dioxide (SnO_2) is a semiconductor with a bandgap of 3.6 eV [46] which makes it transparent in the visible wavelength area. The Fermi energy of ITO lies at 5.1 eV.[47] SnO_2 gets doped with In_2O_3, which causes the necessary vacancies for a higher conduction. ITO is applied as transparent electrode in thin films of a typical thickness of 150 nm. Usually ITO is sputtered on a transparent substrate. Therefor a cost intensive vacuum process is needed which makes ITO an expensive electrode material. Further the obtained thin films are brittle. Another important cost factor is Indium. Indium is a rare earth material and costs 320 €/kg on the world market.[48] To decrease the material costs Indium could be left out from ITO and use only tin oxide as transparent electrode.

Further TCOs are fluorine tin oxide (FTO) for dye-sensitized solar cells and other doped tin oxides.

Grids

As alternative to metal oxide thin films metal grids are studied. Grids can be fabricated photolithographically [50], inkjet printed and electro plated.[52] Depending on the type of deposition grid strucutres can vary from 2 µm line width and grid spacings of 10 µm for photolithographic grids [52] up to 150 µm line width and 8 mm spacing for inkjet printed grids presented in this work.

Carbon nano tubes (CNTs)

Carbon nano tubes have already been successfully applied in displays and photovoltaic devices as transparent electrodes. [53-55] Important for the application of CNTs as TCEs is that the concentration of CNTs needs to be high enough to build a percolation network.[56] To get comparable conductivity properties to ITO the single CNT needs to be more than 100 nm long, leading to high losses in transparency.[57]

Nanowires (NW)

Additionaly various optoelctric devices were made with metal nanowires as transparent electrodes. [58]–[62] NW feature properties similar to CNTs, including threshold concentration for conductivity and related losses in transparency. Although NW feature high conductivities in the wire the wire to wire junction decreases significantly the conductivity. [61] So far the performances of NW thin films rival already those of ITO.[57]

Graphene

As a zero band gap semiconductor graphene comprises electrons delocalized over the whole molecule, offering the possibility to conduct electrons without scattering.[63] Combined with the possible doping of graphene, this leads to high in plane conductivities.[64] In contrast to the high in plane conductivity of graphene stand sheet resistances of up to 800 Ω□. The high sheet resistances are caused by the fact that so far solution processed graphene films consist of thousands of graphene flakes, building up grain boundaries and showing many defects. Nevertheless Wu et al. already showed that solution processed graphene films deliver OLED performances comparable to ITO.[65]

3.2.2 Inkjet printing

Inkjet printing of metal inks is a cheap method for creating conductive structures on various substrates. Metal inks and also almost all layers of an OLED can be inkjet printed. Inkjet printing can be divided in two methods, continuous inkjet printing and Drop-on-demand (DOD) inkjet printing. For DOD inkjet printing either the piezoelectric effect or a thermal process can be used to eject small droplets of ink from the nozzle.[66] The first inkjet printer invented by Hansell 1940 worked with piezoelectric crystals. As shown in Figure 15 in DOD inkjet printers place single drops on the desired position of the substrate.

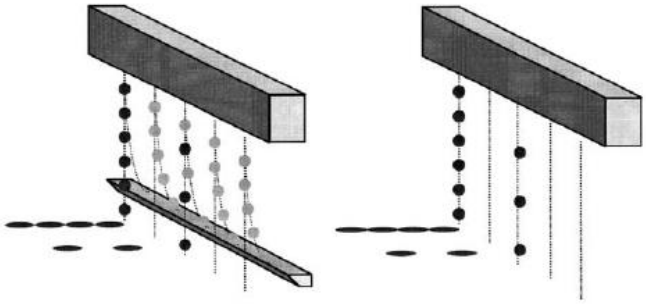

Figure 15: Different types of inkjet printing are shown. Left: Continuous inkjet printing works with partly deflected ink drops. Right: Drop on demand inkjet printing where ink drops are placed exactly.

Continious inkjet printing is a far more material intensive method. In continuous inkjet printing a permanent flow of ink is required. This ink jet is then focused on the substrate for printing and deflected off the substrate for areas which should remain ink free. The deflection of the ink drops works with capacitive coupling. Continous inkjet printers are usually favourable for large area applications and high through put rates. In contrast to continuous inkjet printers DoD inkjet printers can be easily used for experimental laboratories. Hence the major benefit of DoD inkjet printing is that various structures can be digitally drawn and directly printed out on small scale.

Nano particle metal inks

To reduce costs in production of electronic circuits and define easier and cheaper production methods than photo lithography, metal inks were developed for inkjet printing. These inks consist of nano particles which are surrounded by an organic capping to prevent agglomeration. The described particles are diluted in an appropriate solvent. As the inks are applied on the substrates via printing there are special requirments on viscosity, wettability and adheasion.[67] Another important

property of an ink is its dry rate. Fast drying enables fast printing but enhances the risk of nozzle blocking.

To get a conductive structure the printed lines have to be sintered. Sintering can be done in various ways, but all sintering processes aim for the removing of the capping of the nano particles and for linking the nanoparticles to get a bulk like structure. So far nano particle inks do not reach bulk conductivity of the original material.[68]

Piezo electric inkjet single nozzle printhead set up

Figure 16 explains the main parts of a single nozzle printhead, driven by a piezo electric crystal. The nozzle consists of a glass capillary which contains the ink. This glass capillary is surrounded by the piezo electric crystal. On the end are the voltage supply for the piezo crystal and the further ink supply.

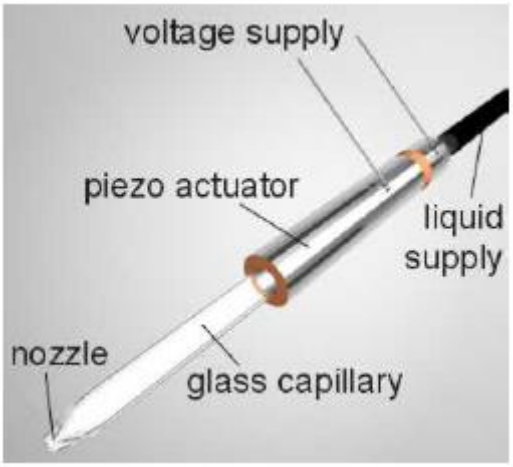

Figure 16: Basic set up of a sinlge nozzle piezo electric inkjet printhead, the ink is in the glass capillary from which it is ejected via the piezo crystal [69].

For printing one drop of ink a voltage is applied on the piezocrystal. The piezocrystal subsequently expands. This causes a shock wave through the glass capillary causing the ejection of an ink droplet. Figure 17 shows an industrial scale printhead based on 128 individually addressable nozzles, each one similar to the described above. The voltage and control plug is on top. The nozzles are at the bottom of the picture. Drop volume of this printhead is 90 pico liter. A print speed of 200 mm/s can be achieved.

Figure 17: Pix Dro LP50 piezoelectric printhead with 128 nozzles at the NTC Weiz used for this thesis.

3.3 Degradation effects of functional groups in PLEDs

As PLEDs should contribute to future lighting applications a long life time is desired. Especially blue emitters are sensible to degradation, because of their large bandgap and therefor low electron affinity. Some of the known reasons for spectral shift in PLEDs are described in the following.

First to mention are Keto-defects in Polyfluorene type materials. Keto defects lead to a strong green shift caused by an Oxygen atom which is added to the polyfluorene chain.[70]

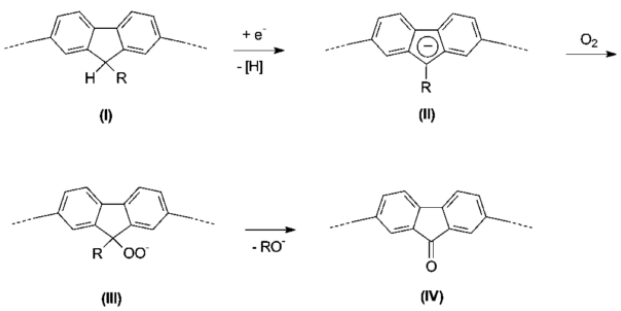

Figure 18: Explaination of the proposed mechanism of the keto defect. 9-monoalkylated fluorine building blocks get (I) get reduced to fluorenyl anions while hydrogen forms. Hydroperoxide (III) anions are formed by the hydrogen and atmospheric oxygen. (IV) finally the hydroperoxide anions rearrange and form fluorenone moieties. This whole process takes place during the synthesis of fluorene type polymers.[70]

As described in the chapter about charge carrier injection, cathode materials with low work function are necessary for a good electron injection. Materials like Calcium (work function ϕ_c=2.9 eV), Barium (work function ϕ_c=2.6 eV) and caesium fluoride (work function ϕ_c=2.2 eV) show low enough work functions, but they also show strong reactivity to Oxygen and humidity. The Aluminium barrier of 150 nm cannot exclude these reactions and interactions sufficiently.[71] For poly(fluorene) type polymers

one possible degradation is explained as a deprotonation reaction of hydroxyl end chain units by diffused Calcium (Equation 8).[72]

$$2\ Ar–OH + Ca \rightarrow 2\ Ar–O^- + Ca_2^+ + H_2$$

Equation 8: Deprotonation reaction of hydroxyl units by diffused Calcium.

Another problem related to moisture are so called dark spots. Dark spots are non emissive areas, caused by delamination of the electrodes. This delamination occurs due to electrochemical dissociation of water according to Equation 9. Driven by the applied voltage water molecules in the device can dissociate causing H and O gas.[73]

$$2\ H_2O + 2e^- \rightarrow H_2 + 2OH^-$$

Equation 9: Dissociation of water under electric fields.

PEDOT:PSS is used in almost all organic light emitting and photovoltaic devices as smoothening layer. Additionally to its smoothing ability the work function of PEDOT:PSS makes it an optimal hole injector, which is desired for high efficient devices. However the drawback of PEDOT:PSS is its acidity. Most times PEDOT:PSS is applied to any surface via spincoating. This leads to a formation of a PSS rich layer on top of the fresh spincasted PEDOT:PSS layer. [36][74] Different studies [75-77] show that PSS causes trap states at the emissive layer, which derives from the acidity of PSS. Another shift in the electroluminescence spectrum is caused by protonation of nitrogen containing polymers.[38] Last to mention are electrophilic addition reactions with unsaturated electron-rich carbon double bonds (e.g. in PPV).[75][78]

4 Experimental methodology

This chapter describes the most important methods used in this thesis. Details of inkjet printing and the used grids are discussed at the beginning. The embedding process for the inkjet printed grids is explained. Further the general OLED fabrication process, for solution processed PLEDs and for vacuum evaporated small molecules is shown. Finally, the used characterisation process and appropriate equipment is described.

4.1 Grid fabrication

All experimental work, except for the sintering of copper grids in formic acid, was done at NTC Weiz Forschungsgesellschaft mbH. Inkjet pringting took place in a chemistry lab under a fume hood. All further preparation steps were carried out in a state of the art ISO-Class 6 clean room facility.

Silver Ink

Here, Cabot CCl – 300 Ag nano particle ink was used. To remove the capping of the nano particparticles and achieve a bulk like grid all inkjet printed silver grids were sintered. The sintering took place in a sinter oven manufactured by Heraeus. In this oven a vacuum can be applied. The printed silver grids were sintered for 2 h at 150°C.

Copper Ink

Two types of copper ink were used in this work. The ink for the embedded copper grids was Intrinsiq Cl-003G. This ink had a lower adheasion on glass and was suitable for embedding. For the over coated grids the ink Cl-005G from Intrinsiq Materials was used. As it was optimized for adhesion, embedding became impossible and it was used for overcoating.

Inkjet printing

Substrates for inkjet printing were cleaned with acetone and mechanically using tissue. This intensive cleaning procedure turned out to be crucial for the later lift off during the embedding process. Further intensive cleaning reduces the possibilities of defects caused by contamination and non emissive areas in the OLED. Printing of the hexagonal grid structures was performed using a PixDro LP50 printer equipped with a FujiFilm Dimatix (Spectra) S-Class 128 nozzle piezoelectric print head. Here, the three previously explained inks were used. Subsequent to printing, the silver grids were annealed for 2h at 150°C in vacuum. Sintering of the silver grids was necessary to stabilise the grid

lines and get a better conductivity. Copper grids were sintered as described in the corresponding chapters. Various grid structures where tested to obtain the dependence of efficiency on grid dimenson. Figure 1 shows the tested grid layouts and the definition of spacing (part f). The smallest grid (a) had a spacing of 1.5 mm and a line width of 90 µm. The grid dimensions were increased from this small size up to a spacing of 8 mm (Figure 1 f). This dimension was the upper limit in size for the used 1x1 inch glass substrates. The first mentioned dimension was the lowest printable dimension, as lower dimensions tend to trickle of and deliver insufficient print pictures. Lower hexagon spacings would have caused blurred hexagons as the printed drops would link to each other. Besides the total spacing also the line width was increased. For the grids up from 3 mm a spacing of 150 µm instead of 90 µm was chosen. Entry d in Figure 1 has the same structure as e, but 2 additional bus bars. This design was made to compare d and e and test the influence of the additional bus bar. Honeycomb structures were used because this design features the least material entry per substrate area. The height of the inkjet printed grid lines was between 300 nm- 400 nm.

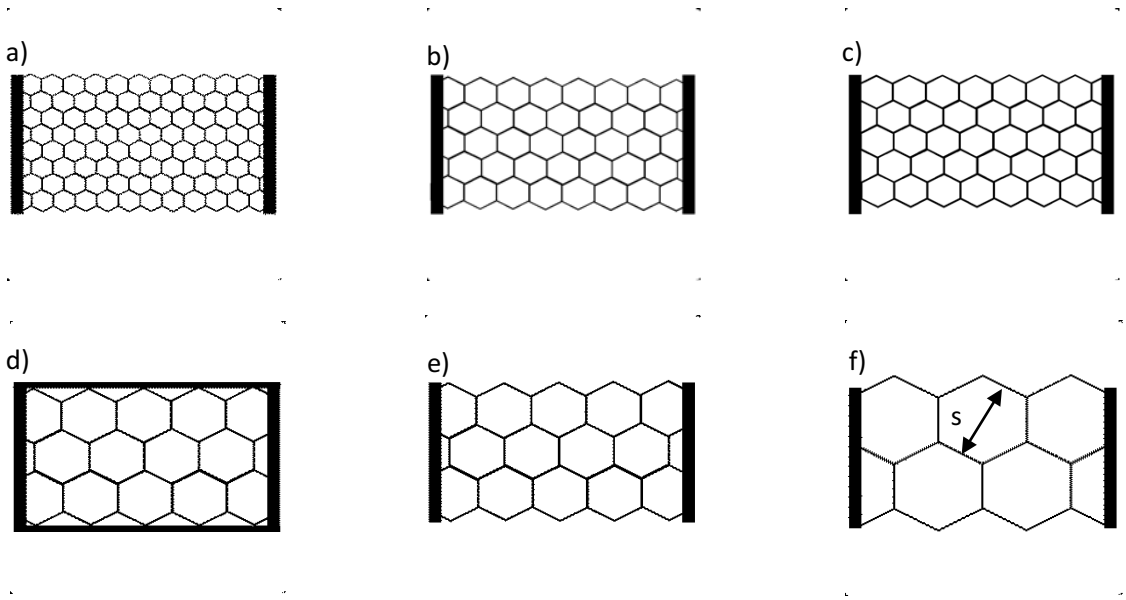

Figure 1: Various grid geometries for inkjet printing; a) 2 mm spacing width 90 µm; b) 3 mm spacing width 90 µm; c) 3 mm spacing width 150 µm; d) 5 mm spacing width 150 µm with busbar; e) 5 mm spacing width 150 µm without busbar; f) 8 mm spacing width 150 µm

Copper ink laser sintering

All copper grids were pre sintered for 90 min at 250 °C in Argon atmosphere. In contrast to the silver ink the capping of the copper ink is more stable. Hence a higher temperature was needed to sinter the lines. This was achieved using an intrinsiq laps-60 class 4 infrared laser with an emitted wavelength of 808 nm. The laser was set to a supply current of 40 A equal to an energy input of 45 W/cm^2.

Copper ink sintered in formic acid enviornment

Alternativeley to the previously described laser sintering some copper grids were sintered in a formic acid atmosphere. Therefor the samples were put in a custom-made sinter oven with the possibility to apply a formic acid atmosphere in the heating chamber. Three identical sets of grids were sintered with 180°C, 200°C and 250°C. Then formic acid was bubbled in the chamber. The formic acid concentration was 3.4% for all samples and the sintering time was 60 min.

4.2 Embedding process

As described in 4.1, inkjet printed lines have a typical height between 300 nm – 400 nm. A typical OLED has a total height of 300 nm – 400 nm. Further feature inkjet printed lines a rough surface. As the mobilities of the charge carriers are strongly field dependent, should the electric field in the OLED be as homogenious as possible for homogenious light emission. [79][80][81][52] From this fact, it is clear that inkjet printed grids offer some problems in the application as TCO. However the grid is fabricated, (photolithographic or inkjet printed) grid lines always tower above the glass substrate and lead to defects in the OLED stacks. These defects can lead to short cuts. To overcome the defects caused by grid lines an embedment can be applied. Here, an embedding process is described, first used by Burgeos et al. [4]. In Ormocomp® embedded inkjet printed silver grids used as TCEs for organic photovoltaic cells (OPVs), showed an increased efficiency of 149% compared to convential OPVs.

UV curable and hybrid Polymers

For the embedding process a UV curable hybrid polymer called Ormocomp® was used. Ormocomp is an Ormocer. Ormocers® were developed by the Frauenhofer Institut für Silicatforschung and are manufactured and distributed by micro resist technology GmbH. [82] These Ormocers ® harden under UV radiation and show glass like properties. UV curable polymers are polymers which change their chemical structure or cross link with neighbouring molecules under UV radiation. Hybrid polymers are polymers with added inorganic elements, for example silicon.

Process

Two substrates are needed for this process, a sacrificial one, on which the grid is printed and a final one, on which the grid is embedded. Figure 20 a displays the first step of the process, inkjet printing of the grids on the sacrificial substrate. Figure 20 b shows the final substrate over coated with the adheasion promoter Ormoprime 08. Ormoprime 08 is the according adheasion promoter for Ormocomp also sustained by micro resist technology GmbH. This adhesion promoter ensures that the cured Ormoprime layer sticks to the final substrate. Before overcoating the substrate needs to be plasma etched to increase the adheasion of Ormoprime08. A drop of Ormocomp is then put on the grid structure (Figure 20 c). At this step it is important to cover the whole grid with Ormocomp to ensure a lift off of the whole grid.

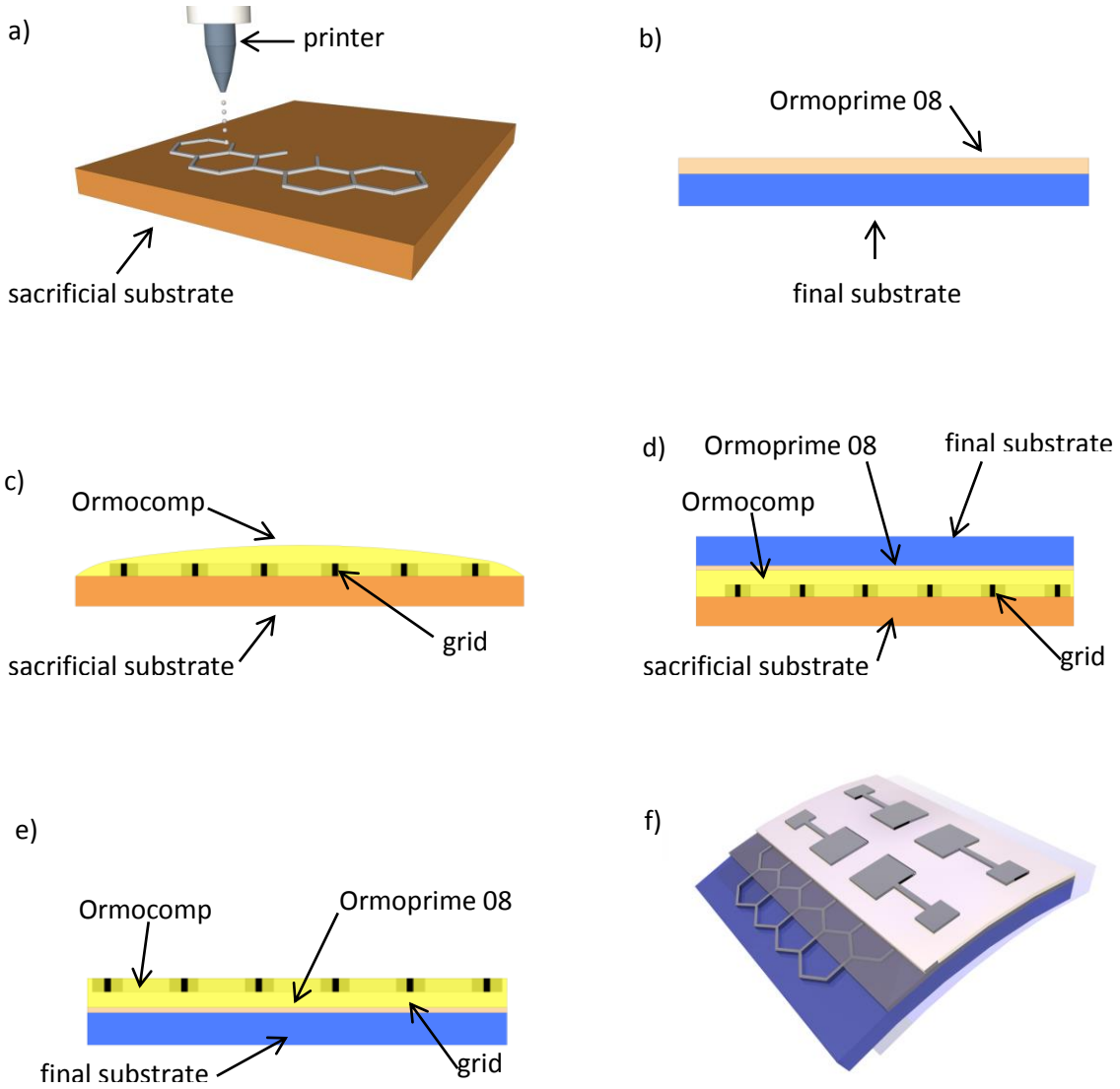

Figure 20: Manufacturing process of inkjet printed embedded grids: a) Inkjet printing of the grid. b) Coating the final substrate with Ormoprime. (blue glass/plastic; beige Ormoprime) c) Covering the grid with Ormocomp. d) Place Ormoprime layer on covered grid. d) Final substrate after lift-off. e) Final stack with finished OLED and structured cathodes.

Afterwards the sample has to be heated on a hotplate to reduce air bubbles in the layer and to promote a better adhesion of the inkjet lines in the Ormocomp. The final substrate is placed on the over coated grid (d). UV radiation (λ_1=280 nm, λ_2=230 nm) was applied to the stack to cure the Ormocomp layer. Finally a lift off is performed and a reverse embedded grid structure was obtained (e). Figure 20 f shows the finished OLED device. The inkjet printed grid is fully embedded in Ormocomp (grey semi-transparent layer). The subsequent layers face a less inhomogeneous surface then on over coated grids. Figure 20 f further shows the active layer (pink) and the finishing Calcium, Aluminium cathode.

4.3 OLED fabrication

The following steps describe the basic fabrication procedure of an OLED, starting with cleaning and plasma etching. Subsequent are the processes for different types of OLEDs are described (solution processed PLED respectively evaporated small molecules).

Cleaning

All sacrificial substrates for inkjet printing had to be cleaned with acetone and mechanically rubbed tissue. The final substrates (quarz glass) were cleaned with acetone and mechanically applied tissue. Subsequentley the glass substrates were sonicated 10 minutes in Isopropanol. The ITO samples were 10 minutes sonicated in Hellmanex, subsequently in Isopropanol. Between each cleaning step the substrates were dry blown with N_2.

O_2 plasma etching

All final substrates were O_2 plasma etched before spin coating with Ormoprime. Plasma etching enhances the wettability of the surface and hence an increased adhesion of the subsequently deposited material is achieved. O_2 plasma etching leads to the formation of OH groups on the surface of the treated sample. The substrates were etched in a femto plasma tool from diener at 200 Watt for 5 Minutes. Grid structures had to be etched shorter (6 s) because the lines showed indications for strong oxidation after a longer etch process. Embedded lines seemed to withstand the etch process better as fewer oxidized areas occurred during the etch process compared to the normal grids.
Also all ITO samples were plasma etched for 5 minutes at 200 W. The sacrificial substrates were excluded from plasma etching, since due to enhanced wettability the applied inks would trickle off. Hence the digital drawn grid structures would not be printed properly.

PEDOT deposition

The grids maintained as described in the sample preparation section where first O_2 plasma etched for 5 minutes at 200 W. A layer of FCE PEDOT:PSS from Clevious was spin coated on the embedded grids. The layer was spun with 2000 rpm for 40 seconds. Subsequently the samples with the FCE layer were baked on a hotplate for 15 minutes under ambient atmosphere. The whole spin coating and drying process was carried out in a laminar flow box. This resulted in an approximately 150 nm thick PEDOT layer.

4.3.1 Solution processed PLEDs

Solution processed HIL

For the solution processed PLEDs, copolymers with various functional units were used. This HIL/LEP systems were first investigated by Nau et al. [38] Figure 21 displays the various chemical groups of the Copolymers. The different groups were added with different focus on hole injection, hole transport, recombination and groups to prevent the copolymers from degradation in the acidic environment of PEDOT. The HIL had on its polymer chains the functional groups A (indenofluorene) E (triphenylamine) in a ratio of 50:50.

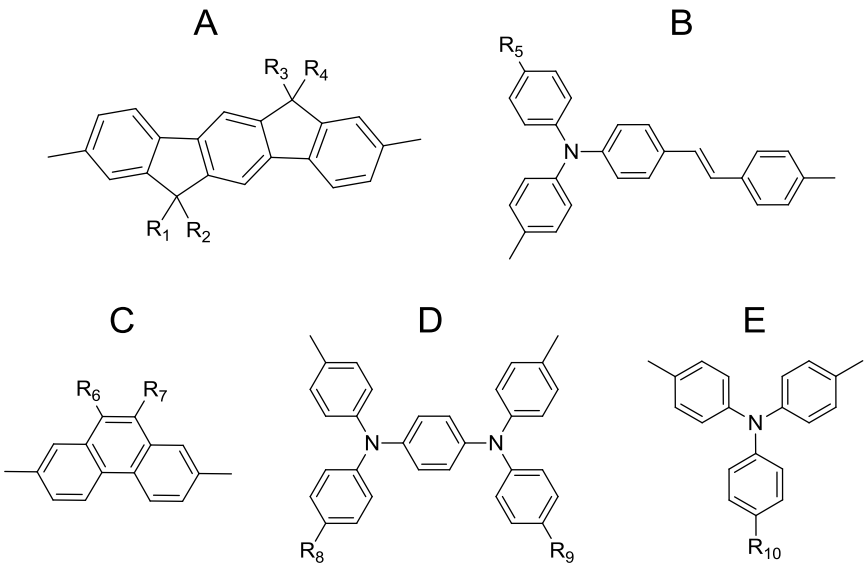

Figure 21: Chemical structures of the individual copolymer building blocks: A) 9,9,12,12-tetraorganyl-6,12-dihydroindeno[1,2-b]fluorene; B) (E)-4-organyl-N-phenyl-N-(4-styrylphenyl)aniline; C) 9,10-diorganyl-phenanthrene; D) N^1N^4-bis(4-organphenyl)-N^1,N^4-diphenylbenzene-1,4-diamine E) 4-organyl-N,N-diphenylaniline

Solution processed LEP

The LEP consisted of ABCD. In detail the emissive units are indenofluorene (A), (E)-4-organyl-N-phenyl-N-(4-styrylphenyl)aniline as an emissive unit (B), electron-transport-supporting phenanthrene (C), and hole-transport-supporting amine (D) units at an A:B:C:D ratio of 46:2:50:2.

Preparing solutions

For the solution processed PLEDs also a solution processed HIL was applied. The hole injection layer (HIL) and the light emitting polymer (LEP) were dissolved in Toluene. For the HIL a concentration of 2 g/L and for the LEP a concentration of 4 g/L was chosen.

Layer Deposition

Layer deposition of the solution processed HIL and LEP were carried out in an Argon filled glovebox. A 20 nm thick HIL and a 60 nm thick LEP layer were spin coated on the FCE layer. This was achieved by spinning the HIL solution with 1000 rpm for 15 seconds and subsequent with 3000 rpm for 40 seconds. The LEP was spin coated with 1500 rpm for 15 and subsequent with 3000 rpm for 40 seconds.

The HIL was baked under Argon atmosphere on a hotplate at 200°C for one hour. The LEP layer was baked under high vacuum at 120°C for one hour.

4.3.2 Thermal evaporation of OLEDs

The steps here describe the materials, methods and hardware for thermal evaporated OLEDs. First are the used materials explained.

Evaporated HIL

For the experiments with the thermal evaporated OLEDs on embedded grids the standard HIL N,N-Di(1-naphthyl)-N,N-diphenyl-(1,1-biphenyl)-4,4-diamine (NPB) from sigma Aldrich was used. A 30 nm thick film of NPB was evaporated on the PEDOT:PSS layer with the embedded grid underneath. Figure 22 shows the molecular structure of NPB.

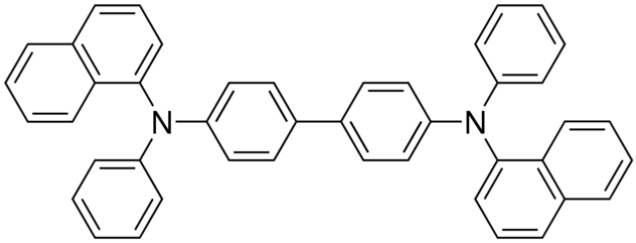

Figure 22: NPB molecular structure taken from [10].

Evaporated LEM

Tris-(8-hydroxyquinoline)aluminum (Alq3) is a commonly used thermal evaporated LEM. It is easy to handle in thermal evaporation and well studied, therefore it is perfectly suited for studying TCEs. For the molecular formula see Figure 12. 300 nm of Alq3 were applied on the previous NPB layer with the vacuum evaporation chamber described in 4.3.2.

Thermal evaporation

For the evaporated hole injection layer (HIL) and the evaporated light emitting layer (LEM) a vacuum deposition chamber in an argon filled glovebox was used. This same chamber was also used for the

deposition of the Calcium and Aluminium layers, which have been evaporated through a mask. The chamber consists of 5 different evaporation units. To realize a fully evaporated OLED the chamber was built with a rotatable sample holder wheel and a rotatable mask wheel, hence it is possible to evaporate different material layers with different masks without breaking the vacuum. The whole process is software controlled. The devices for thesis were fabricated according to the following steps:

The inkjet printed grids were embedded according to the process in 4.2. Then they were spin coated with F CE PEDOT as explained in 4.3. Then the samples were transferred into a glovebox with the vacuum evaporation chamber. The chamber was vented and opened. The evaporation units for the organic materials had a crucible in a heating set up. The crucible were filled with Alq3 and NBP, respectively and then brought in two different units. Calcium and aluminium were evaporated from tungsten boats in two further units. When all the materials were located the samples were put in the substrate holder wheel with the mask wheel underneath. Finally the chamber was closed and evacuated to 10^{-6} mbar. NPB and Alq3 were evaporated over the whole substrate area. To define the OLED size calcium and aluminium were evaporated through masks.

Cathode

To enhance electron injection 10 nm of Calcium were evaporated through a mask on the Alq3 layer. To cover up the OLED and get a good conductivity 100 nm of Al were evaporated through the same mask with the vacuum chamber described in 4.3.2. The final cathode consisted of 10 nm evaporated Calcium and subsequently 150 nm evaporated Aluminum, as described.

4.4 Characterisation methods

In the following the various methods for characterising grids and OLEDs are explained. It is important to gather information about the grids themselves to understand the influences on the later processed OLED on the grid. Microscopy was performed to check the grids for cracks. Optical transmission measurements of the grids were necessary to compare the different geometries in transmission and with ITO. With SEM, AFM and profilomter measurements the microscopic influence of the embedding process was revealed. Finally the OLEDs were electro-optically characterised, to compare the different influence on different geometries on the performance.

Optical microscope measurements

As the grids were printed with line widths in the µm range and spacings up to the mm range optical microscope pictures were taken with an Olympus 2000 microscope. Distances in the microscope pictures were measured with the cell^D scan software. An optical microscope can be used in various modes. For this thesis most pictures were taken in reflective mode. To increase the contrast of obstacles and planar inhomogeneity pictures were also taken in dark mode.

Optical transmission measurements

First it is necessary to mention that a grid has no exact transmission. The grid lines block almost all the light. In between the grid lines all the light is passing through. Therefor a so called “coverage” in percent was introduced. It is the ratio of grid line area divided by the whole area covered by the grid. The calculation is described in Equation 10.

$$\frac{A_g}{A_w} = c\ (\%)$$

Equation 10: A_g…area covered by grid lines; A_w…total grid area

For grid spacings up to 5 mm spacing transmission measurements were performed according to Equation 11.

$$T(\lambda) = \frac{I(\lambda)}{I_0(\lambda)}$$

Equation 11: T…transmission; I…intensity; I_0…incident intensity

Transmission is defined as transmitted intensity (I(λ)) divided by incident intensity (I_0(λ)). I is a function of the wave length λ. Hence transmission depends on the wavelength of the incident light. To measure the wavelength dependent transmissions the spectrometer needs to have a tuneable light source. Most spectrometer consist therefore of a broad band light source which emits all wavelengths. To tune the wavelength a spectrometer uses either a prism or a grating. To characterize the grids a perkin elmer lambda 900 UV/VIS spectrometer was used. It consists of a Deuterium and Halogen lamb as a light source and holographic gratings for tuning the wavelength. The whole measurement system is fully software controlled.

Profilometer measurments

A profilometer measures the surface topology of a material. Main parts are a cantilever with a needle and a coil for vertical measurements and a moveable sample stage. The measurement is done by a needle which is scratching over the surface while the sample stage is moved underneath. The vertical displacements of the needle are measured inductive with a coil attached to the cantilever. The lateral position and the vertical amplitude are mapped and a surface profile can be determined. For this thesis a Bruker XT profilometer was used. It can achieve a vertical resolution down to 1 nm up to 1 mm depending on the needle. Lateral it can measure up to an area of 55 mm times 55 mm.

Device Characterisation

The completed OLED/PLED deviceses were characterized with following tools. Voltage-current characteristics were recorded with a KEITHLEY 2612 sourcemeter (computer assisted). Simultaneous measurement of the emitted light intensity was performed using a silicon-diode and a KEITHLEY 6417A electrometer. Photocurrent – luminance calibration was done with a MINOLTA LS-100 luminance meter.

With the calibrated photocurrent luminance ratio the luminance was calculated according to Equation 12. The luminance was measured at a constant photocurrent A_c for this calibration.

$$lum[cd/m^2] = photocurr.[A] * \frac{lumi(A_c)[cd/m^2]}{photocurr.(A_c)[A]}$$

Equation 12: lum...luminescence; photocurr...photocurrent; lumi(Ac)...luminescence at calibration photocurrent; photocurr.(A_c)…photocurrent during calibration

According to Equation 13 the current density through the device was calculated. A is the active area of the OLED.

$$curr.density\ [A/m^2] = \frac{curr[A]}{A[m^2]}$$

Equation 13: curr. density…current density, curr…current, A…active area

The luminance in combination with the current density can reveal the efficiency of the OLED according to Equation 14.

$$eff\ [cd/A] = \frac{luminance[cd/m^2]}{current\ density\ [A/m^2]}$$

Equation 14: eff…efficiency

Another important property of a light emitting device is the emission spectra. Measurement of the electroluminescence emission spectrum was done using a LOT-ORIEL CCD-spectrometer.

5 Solution processed reference PLEDs on ITO

This chapter introduces basic PLEDs on ITO. The PLED was fabricated according to the process given in chapter 4. The characterisation comprises the voltage-current-luminescence characteristics and electroluminescence spectra. Figure 23 displays the voltage-current-luminance characteristics and the electroluminescence spectra of the devices. The current density and luminance increase exponentially from the onset. The characteristics also displays a low current density in reverse bias. The graph of the current density (circles) shows a smooth increase without spikes. This leads to the conclusion that there are few shorts in the device.

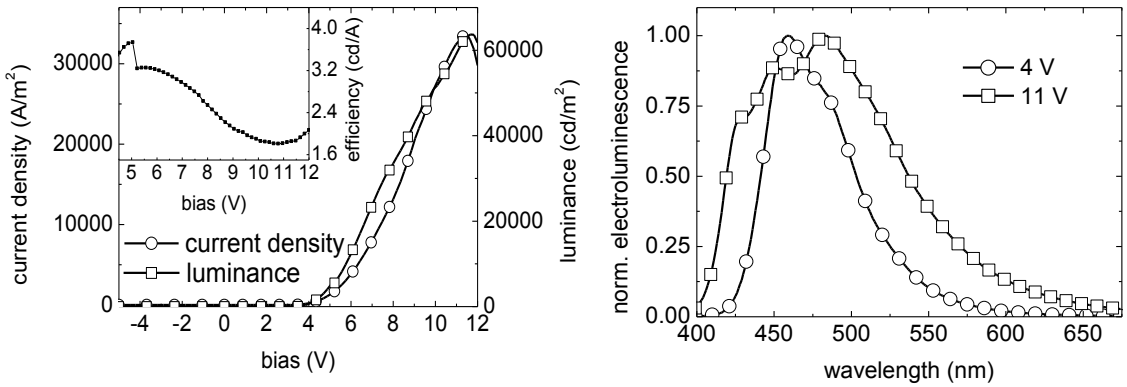

Figure 23: Right: Voltage-current-luminance characteristics of PLEDs (ITO/PEDOT:PSS/HIL/LEP/Ca/Al) on ITO. Right: Normalized electroluminescence spectrum of PLEDs at 4 V operating voltage (circles) and 11V (squares).

The onset is at 3.6 V as typical for this material with this layer thickness. The efficiency reached a value of 3.7 cd/A. The efficiency at 1000 cd/m^2 was 3.2 cd/A. A maximum luminance of 64000 cd/m^2 was reached. The current density at this voltage reached a maximum of over 30000 A/m^2. The electroluminescence spectra are stable at low voltages and corresponding low current densities. With increasing current density a peak shift to the red take place. An increasing of the peak at 480 nm is visible. Compared to the spectra in chapter 6,7 and 8 the current density at 11 V for the ITO devices is more than 3 times higher. This results in a higher stress on the material. Caused by this stress is a far higher spectral shift in the electroluminescence spectrum.

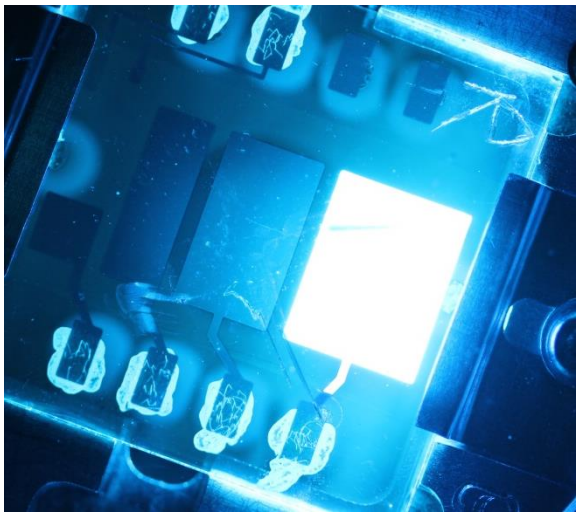

Figure 24: Image of a PLED processed on an ITO substrates.

Figure 24 shows an image of the described PLED under operation. Also visible are the not operating neighbouring cathodes in different sizes.

The here presented devices are used as references for the grid devices.

Figure 25 shows the outcome of ultraviolet photoelectron spectroscopy (UPS) performed by Nau et al. [38] Here the reasons for the high efficiencies of the PLED consisting of the used copolymers (CP) become clear. PEDOT:PSS has a work function of 5.0 eV and the HIL an ionisation energy of 5.5 eV. Therefore easy hole injection and electron blocking is possible. The HOMO of the HIL is further only 0.3 eV away from the HOMO of the LEP leading to a low hole injection barrier. Additionally the LUMOs show an energy barrier of 0.2 eV for electrons. The energy barrier for electrons at the PEDOT:PSS HIL interface is with 2.4 eV high enough for sufficient electron blocking.

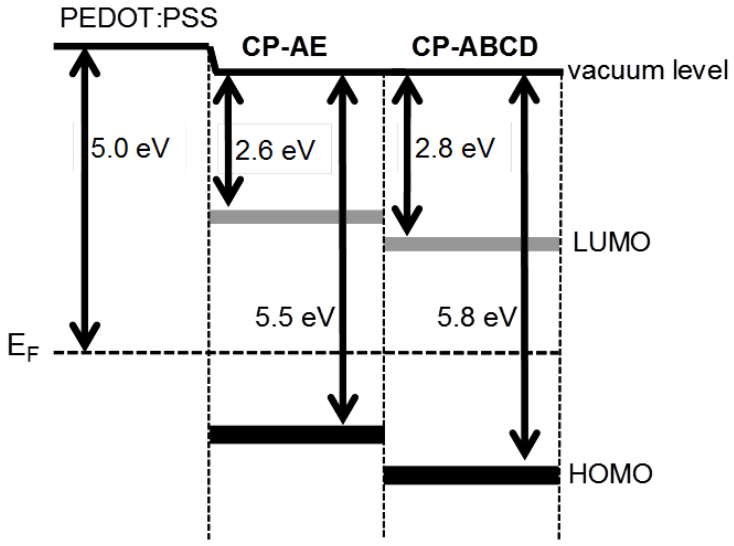

Figure 25: Band diagramme of PEDOT:PSS/HIL/LEP of the presented PLED. Taken from [38].

6 OLEDs based on inkjet printed silver grids

The following chapter comprises grids printed with the silver grid described in 4.1. In the beginning optical characterization of the grids, ITO and Ormocomp® are presented. Further PLEDs on overcoated and embedded grids are shown.

6.1 Optical characterization of grids

As explained in 4.4 it is impossible to measure an exact transmission or absorbance of a metal grid. Nevertheless, as long as the measuring spot size exceeds the grid spacing, an approximated average transmission value can be estimated. The here presented transmissions are measured on grids with sufficient small spacing. These data was measured with a PerkinElmer Lambda 900 UV/VIS – spectrometer. According to Equation 11 I_0 was obtained by measuring the transmission of an empty glass sample. Subsequently the grid structures were put in the sample holder and measured.

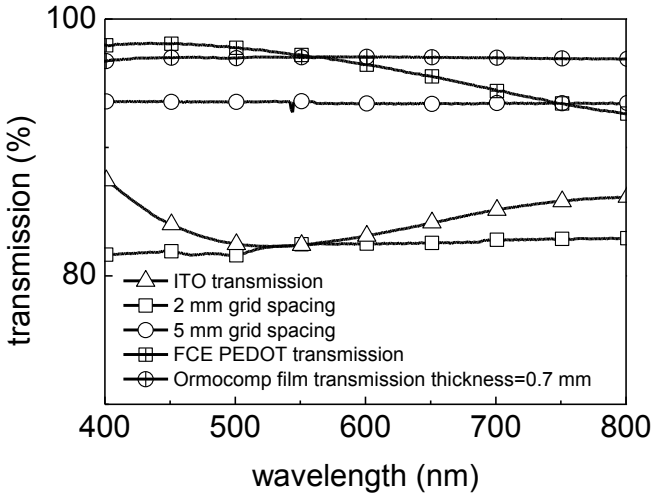

Figure 26: Optical transmission of: 2 mm spacing grid, 5 mm spacing grid, ITO, FCE PEDOT:PSS and an Ormocomp thin film.

Figure 26 shows the transmission of the used materials and grid spacings. A grid with a spacing of 2 mm (empty squares) is already fine enough meshed to be comparable to ITO (empty triangulars). The wider the grid spacing gets the higher gets the transmission. This stems from the fact that a higher spacing leads to a lower coverage and thus lower shadowing. With a spacing of 5 mm (empty circles) one can achieve an average transmission of almost 92%. This lies also above the transmission of ITO (empty triangulars) with 88% on average. Also important for later OLED performances is the transmission of Ormocomp (circles with cross). It has an average transmission of 97% which is comparable to glass. Further the graph displays the transmission of a 150 nm thick F CE PEDOT layer.

Transmission is between 98% blue wavelength range and 92% in the red range. From Figure 26 it is furthermore evident that the transmission of grids is constant over the visible wavelength region. The transmission of ITO varies strongly depending on the wavelength.

6.2 PLEDs manufactured on inkjet printed silver grids

Grids with a line width of 150 µm and a spacing of 3 mm were investigated in this part. The first ink used was silver nano particle ink (chapter 4.1). Before processing the OLED layers on the grid the grid lines were investigated with a Dektatak Stylus profilometer. Subsequent to the profilometer measurments the OLEDs were processed on the grids and characterised. The results are following. To compensate the grid line height and reduce subsequent defects a special formulation of PEDOT:PSS was used for this grids. F CE PEDOT:PSS produced and delivered by Clevious is a special formulation of PEDOT:PSS, designed to make thick layers and hence overcoat inkjet printed structures.

Profilometer measurments

Figure 27 shows one of the profilometer measurements, it is a cross-section through a grid line on a glass substrate. This figure is representative for all the silver grid lines as no modifications in the printing set up or adjustment have been made.

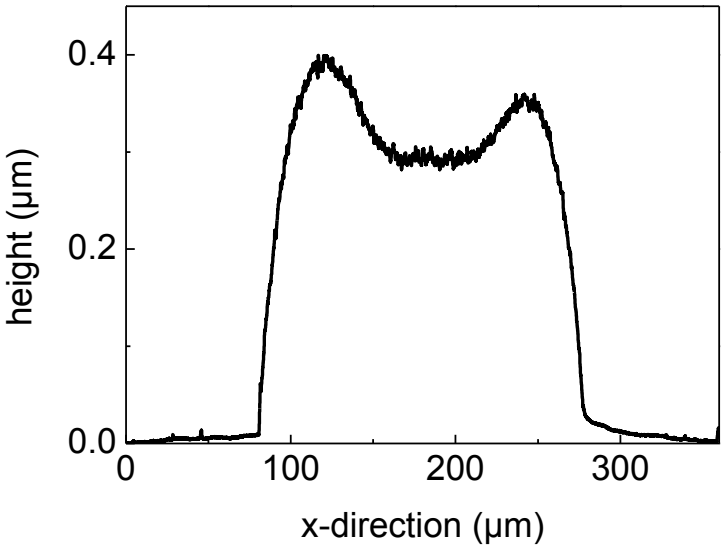

Figure 27: Profilometer measurement of Ag grid line on glass.

The grid line height is between 300 nm and 400 nm, which exceeds the total stack height of the fabricated PLED (150 nm PEDOT, 20 nm HIL, 60 nm LEP, 10 nm Ca, 150 nm Al). As mentioned in chapter 4 the lines also show a rough surface.

6.2.1 Device characteristics of over coated grids

Figure 28 shows the voltage-current-luminance characteristics of the OLED devices with overcoated grid lines. The onset is at 3.6 V typical for this material with this layer thickness. A maximum luminance of 16000 cd/m^2 was achieved. The current density reaches a value of 10000 A/m^2. From this data a maximum efficiency of 3.4 cd/A was calculated. The current density graph does not show significant spikes due to overcoating. This device has already a comparable performance to the previously measured ITO device. The second picture in the graph shows the normalized electroluminescence spectrum. The spectrum is sufficient stable over the whole operating voltage area. Peak broadening is smaller for the ITO device in chapter 5 because the current density for this device at 7 V is 30 times smaller than for ITO, which results in a lower stress of the material.

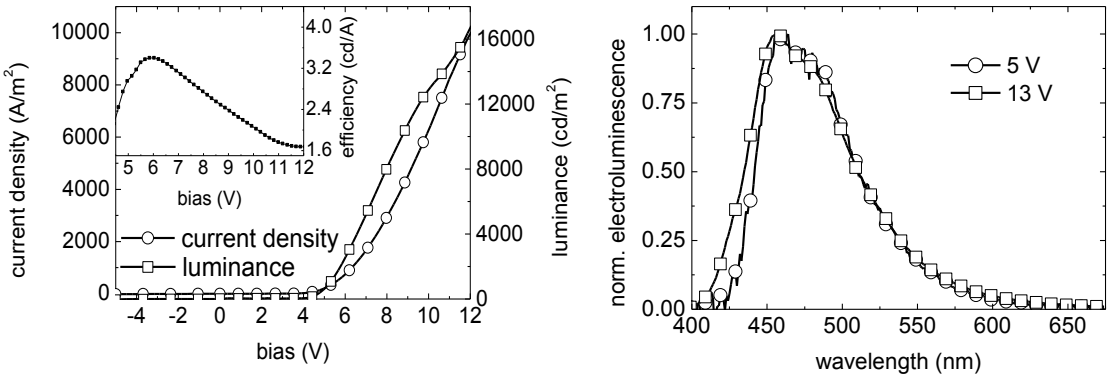

Figure 28: Left: Voltage-current-luminance characteristics of over coated grid with 150 µm line width and 3 mm line spacing. Right: Electroluminescence spectra at 5 V (open circles) and 13 V (open squares).

Figure 29 displays the cut-off current of two PLED devices. One has ITO (open triangles) as bottom electrode and the other an over coated grid (open aquares with cross). A significant discrepancy of the cut-off current is visible. The cut-off current is 3 orders of magnitude higher, either under reverse or forward bias. It is suggested that this behaviour derives from shorts caused by the high grid lines. To flatten and planarize the electrode an embedding process was applied in the following.

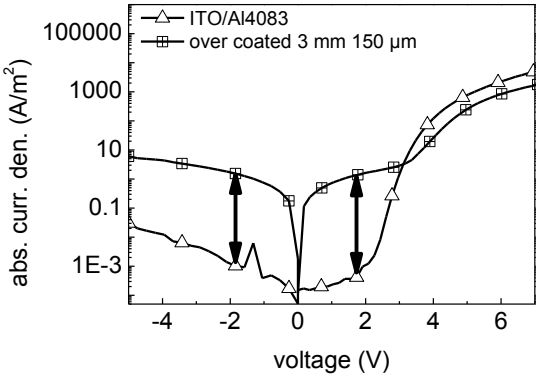

Figure 29: Logarithmic plotted cut-off current of a PLED fabricated on an over coated grid (square with cross) and on ITO (open triangles)

6.3 Inkjet printed embedded Ag grids with solution processed HIL and LEP

As shown in the previous chapter inkjet printed grids as transparent conductive electrodes already showed a sufficient performance. Still, compared with the ITO device from chapter 5, the high maximum luminance values of ITO were not reached. Further was the device yield of the so far tested structures low. Many devices showed an ohmic behaviour in the I-V characteristics. As shown in Figure 29 the cut-off current is 3 orders of magnitude higher in the grid based devices compared to the ITO based devices. To improve the overall performance of the grid lines the previously described embedding process was applied. This part presents embedded inkjet printed silver grids with various dimensions. Grids with a line width of 90 µm and 1.5 mm, 2 mm and 3 mm spacing were tested. Further grids with 150 µm line width and 3 mm, 5 mm and 8 mm were investigated. Additionally to the normally used 5 mm grid, a 5 mm grid with an extra busbar on each side was tested. To get comparable results the same solution processed PLEDs as in the previous chapters were manufactured in the same way. Subsequently to printing the grids were embedded as described in chapter 4 and the embedded lines were investigated with a Profilometer. Figure 30 displays a cross-section of an inkjet printed line embedded in Oromocomp. The height levels of Ormocomp and grid almost match. Important to notice is that the grid line may lay under the Ormocomp level (about 40 nm). A ditch between Ormocomp and grid line, which occurred in all measurments can be found. This ditch derives from shrinking. Ormocomp shrinks up to 10% under UV radiation. The surface of the grid line becomes even rougher after the lift off.

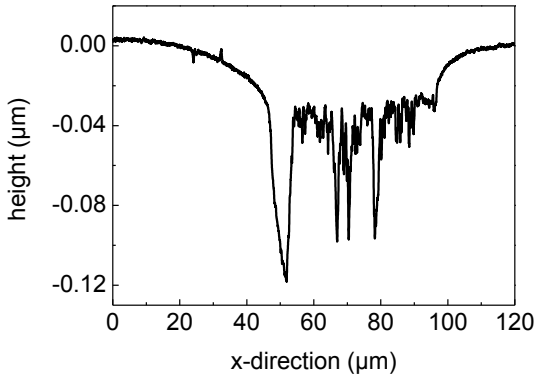

Figure 30: Profilometer measurement of embedded silver line after lift off, left and right is Ormocomp, in the middle is the silver line with spikes.

Figure 31 shows that these spikes smooth under a layer of PEDOT:PSS. Still the ditches between the Ormocomp and the grid line remain, but smaller. The high peak to the right is related to PEDOT spin

coating. As the ditch lies next to the peak it is assumed that the ditch builds an obstacle for drops of PEDOT:PSS caused by the small surface gap and according surface energy differences.

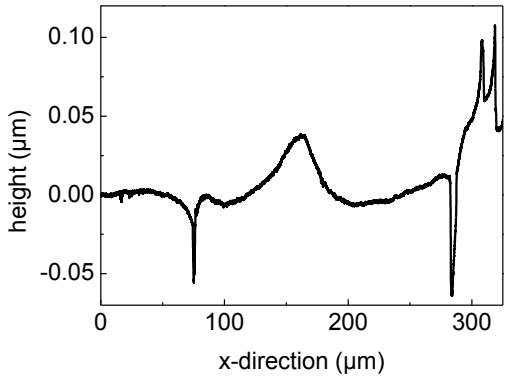

Figure 31: Profilometer measurement of embedded and PEDOT:PSS overcoated grid line.

6.3.1 Device characteristics of embedded grids

The over coated grids already showed a comparable performance to ITO based devices. To further increase the performance the next series of grids were embedded. Further the grid structures were varied to test for an optimal grid dimension. Figure 32 shows the voltage-current-luminance characteristics of the first device. It has a grid with a spacing of 1.5 mm and a line width of 90 µm.

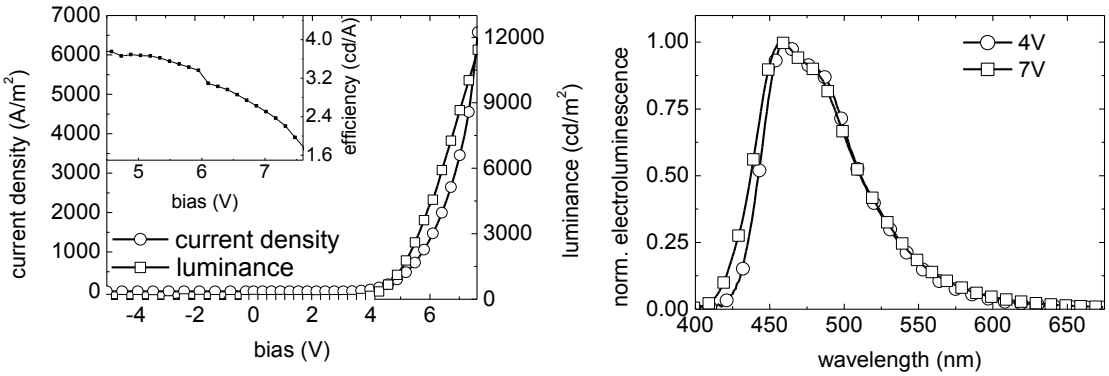

Figure 32: Left: Voltage-current-luminance characteristics of a PLED on an embedded silver grid with 1.5 mm grid spacing and 90 µm line width. Right: According normalised electroluminescence spectrum.

The onset is at 3.6 V. The current density and luminance graph show a smooth line. Further the current density under backward bias is low. The inset presents the efficiency of the OLED. The maximum efficiency is approximately 3.8 cd/A. The efficiency at 1000 cd/m^2 is 3.7 cd/A which is close to the maximum efficiency.

Figure 33 presents the data of a grid with 2 mm spacing and a line width of 90 µm. This grid shows the same onset at 3.6 V. This grid structure delivered a slightly higher maximum luminance at even

lower voltages then the previous grid. The increase of luminance and current density in the voltage range from 4 V to 6 V is steeper than for the grid with 1.5 mm spacing.

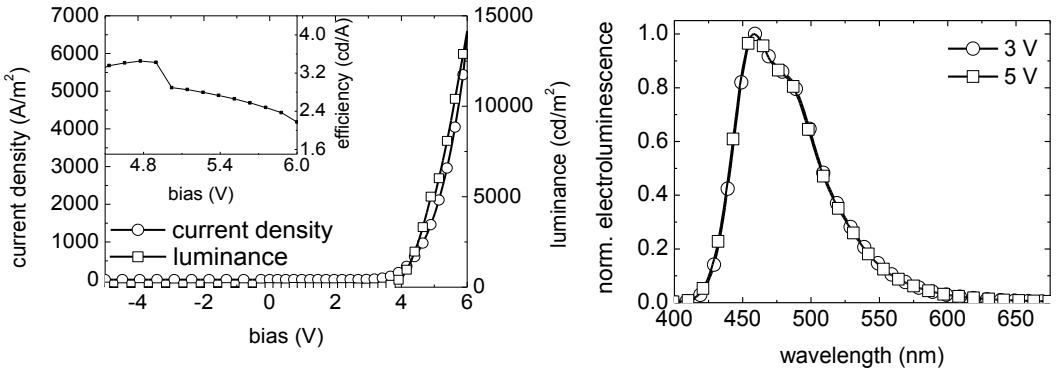

Figure 33: Left: Voltage-current-luminance characteristics of a PLED on an embedded silver grid with 2 mm grid spacing and 90 µm line width. Right: According normalised electroluminescence spectrum.

The maximum current density is 6500 A/m^2. The maximum luminance reached a value of 14500 cd/m^2 at an operating voltage of 6 V. Maximum efficiency was 3.5 cd/A and efficiency at 1000 cd/m^2 was 3.0 cd/A. The electroluminescence spectra are colour stable. For the operating voltages of 4 V and 5 V no peak shift occurs. This might derive from the low current density of 2000 A/m^2 at 5 V.

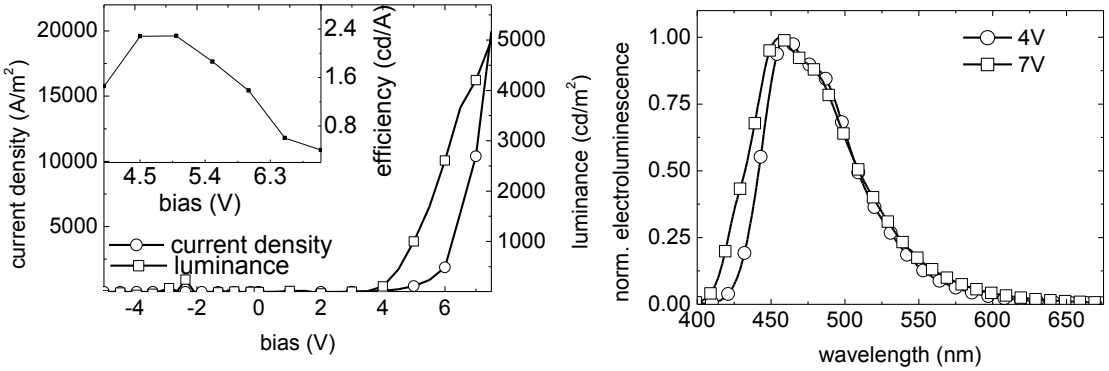

Figure 34: Left: Voltage-current-luminance characteristics of a PLED on an embedded silver grid with 3 mm grid spacing and 90 µm line width. Right: According normalised electroluminescence spectrum.

Figure 34 shows the characteristics of a grid with a spacing of 3 mm and a line width of 90 µm. The spacing is bigger compared to the previous grids. Line width stays the same at 90 µm. This leads to a lower maximum luminance of 5000 cd/m^2. Further, the current density increases in the small voltage range from 4 V to 7.5 V to a maximum value of 19000 A/m^2 which leads to a worse current efficiency of 2.3 cd/m^2. The maximum current efficiency is equal to the efficiency at 1000 cd/m^2. The turn on voltage stays the same at 3.6 V indicating the approximately same layer thicknesses. At approximately -2 V a small outburst of the luminance is visible. This can be a measured artefact or a defect break down. On the right of Figure 34 the corresponding electroluminescence spectrum is

visible. According to the high current densities a peak broadening into the blue occurs due to degradation because of the PSS interaction with the vinylene unite of the light emitting copolymer (CP). [38]

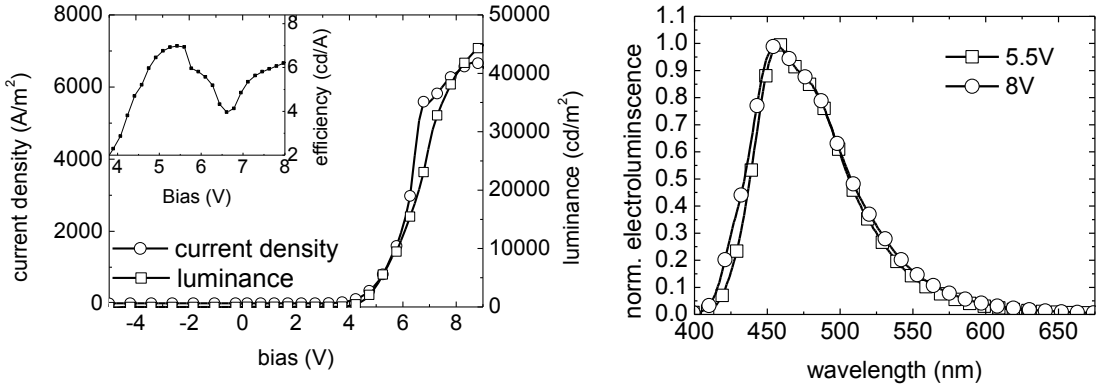

Figure 35: Right: Voltage-current-luminance characteristics of a PLED on an embedded silver grid with 3 mm grid spacing and 150 µm line width. Right: According normalised electroluminescence spectrum.

Figure 35 shows voltage-current-luminance characteristics of a grid with the same spacing (3 mm) as the previous one, but here the line width is broadened to 150 µm. Luminescence values up to 45000 cd/m^2 for embedded inkjet printed silver grids were achieved. The maximum current density reached a value of 6700 A/m^2. Maximum efficiency was calculated to 7 cd/A and efficiency at 1000 cd was 5.2 cd/A. At approximately 7 V is kink in the current density and the fast rise in current density stops. Saturation occurs and charge carrier limited current flow is reached. Shortly after the saturation in current density is reached, the luminance saturates also. Electroluminescence spectra remain sufficient stable from 5.5 V to 8 V.

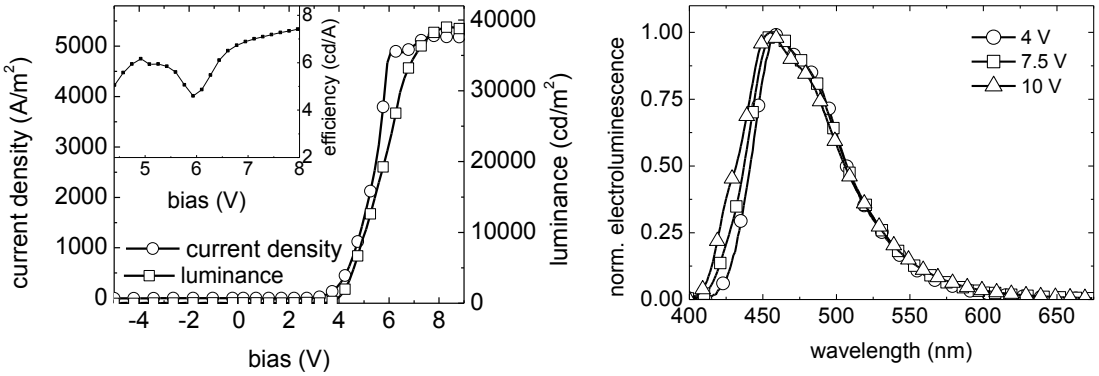

Figure 36: Left: Voltage-current-luminance characteristics of a PLED on an embedded silver grid with 5 mm grid spacing and 150 µm line width, additionally this grid has 2 extra bus bars on each side. Right: According normalised electroluminescence spectrum.

Figure 36 shows the characteristics of a device with the same line width of 150 µm but now with a spacing of 5 mm and an additional busbar around the grid (compare Figure 19, d). A maximum current density of 5000 A/m^2 and a maximum luminance of almost 40000 cd/m^2 were achieved.

Efficiency at 1000 cd/m^2 was calculated to 3.5 cd/A while the maximum efficiency was determined to 6 cd/A. Saturation in current density is again present at app. 6 V. In Figure 36 (right) are plotted the electroluminescence spectra at 4 V, 7.5V, and 10 V. A peak broadening to the blue occurs. This peak broadening is related to a shift of the recombination zone towards the HIL.[38]

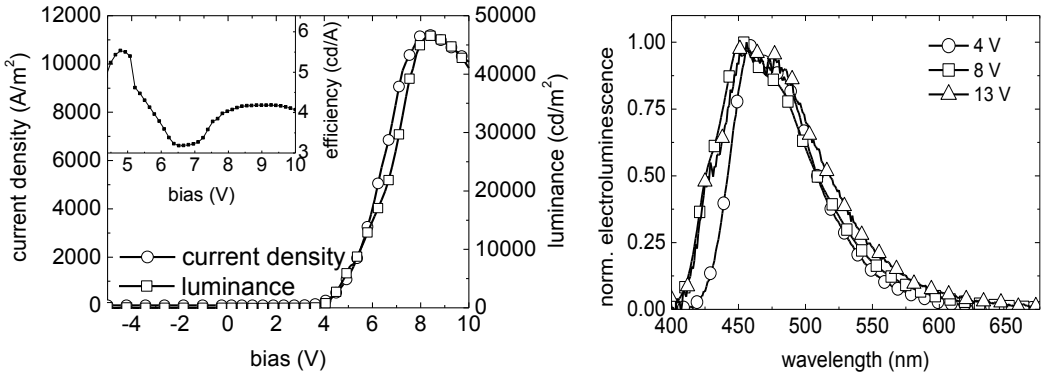

Figure 37: Left: voltage-current-luminance characteristics of a PLED on an embedded silver grid with 5 mm grid spacing and 150 µm line width. Right: According normalised electroluminescence spectrum.

Figure 37 shows the voltage-current-luminance characteristics of the same line structure as the previous grid, except this grid had no extra bus bar. This grid structure exhibits a higher maximum current density of 11000 A/m^2 compared to the previous one although two conducting lines are missing. With this grid dimensions of 5 mm hexagon spacing and 150 µm line width the highest luminescence values for inkjet printed silver grids were achieved with 47000 cd. The maximum efficiency was calculated to 5.5 cd/A and the efficiency at 1000 cd/m^2 was 4.2 cd/A. The electroluminescence spectra are on the right in Figure 37. One spectrum was taken at the so far highest operating voltage for spectra, at 13 V. The peak broadening can be again realted to a shift of the recombination zone.[38]

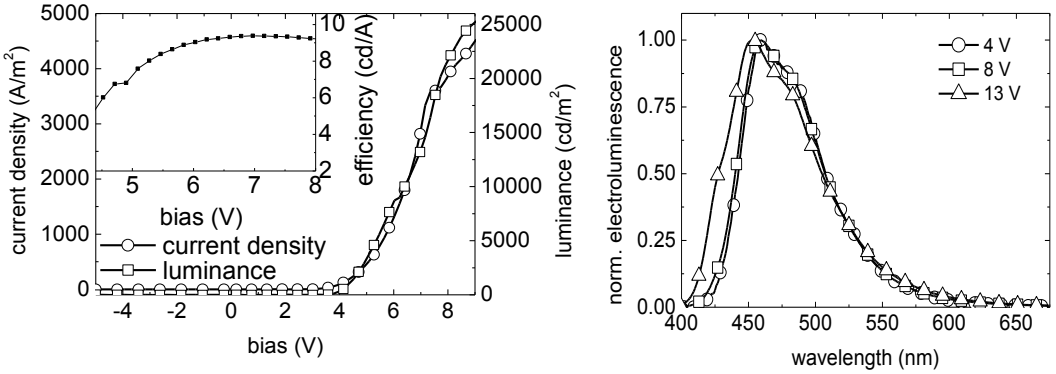

Figure 38: Left: Voltage-current-luminance characteristics of an embedded silver grid with 8 mm grid spacing and 150 µm line width. Right: According normalised electroluminescence spectrum.

Figure 38 shows voltage-current-luminance characteristics of the biggest tested grid structure with a spacing of 8 mm and a line width of 150 µm. This grid structure displays the best efficiencies of more than 9 cd/A. The maximum current density was measured 4500 A/m^2. The efficiency at 1000 cd/m^2 was calculated 7 cd/A. Maximum luminance was determined to be 26000 cd/m^2. The electroluminescence spectrum reveals again the influence of PSS. The peak broadening is clearly visible.

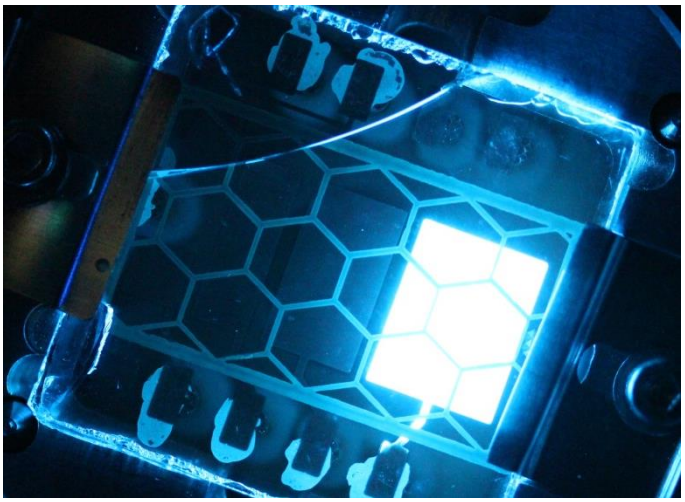

Figure 39: Working PLED on embedded grid with 5 mm spacing and 150 µm line width.

Figure 39 displays a PLED under operation. The grid had 5 mm spacing and 150 µm line width. This grid disposes the additional bus bars on the sides.

6.4 Inkjet printed embedded silver grids with vacuum evaporated HIL and active layer systems

As the experiments with solutions processed PLEDs on embedded inkjet printed silver grids were promising an alternative OLED manufacturing process should be tested. This part of chapter 6 deals with thermal evaporated materials as HIL and active layer as small molecules are industry state of the art materials. As described in 4.3.2 NPB was used as HIL. 30 nm of NPB were deposited with the process described in 4.3.2. 150 nm of Alq3 were deposited on the HIL without breaking the vacuum of the evaporation chamber. Subsequent to processing the OLEDs were characterised as explained in 4.4. Here the characteristics are presented.

Device characteristics

Figure 40 shows the current-voltage-luminance characteristics of the described device. The ohmic behaviour is significant over the shown voltage range. This behaviour might result from shorts. Due to the thermal evaporation process small molecules reconstruct surface topologies of under laying substrates leading to shorts.[83] Due to this behaviour current densities vary from 3700 A/m^2 at -9 V and 5000 A/m^2 at 13 V. The luminance was almost impossible to measure as the maximum value is only 180 cd /m^2. Due to the low luminance, it was impossible to record reliable spectra of this device.

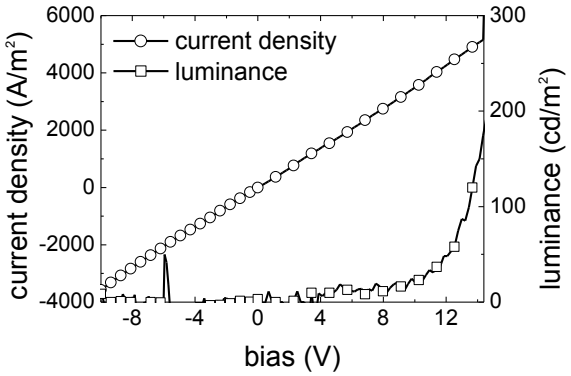

Figure 40: Voltage-current-luminance characteristics of OLED on embedded Ag grid with evaporated HIL/EML system.

The characteristics of different grid geometries showed all the same behaviour as in Figure 40. In conclusion thermal evaporated OLED materials seem to perform worse on embedded silver grids then solution processed PLEDs. During a thermal evaporation process the evaporated material sticks immediately to free surface spots. A further movement and migration of the molecuels can be excluded. Therefore small molecules build perfectly conform layers of the substrate underneath,

including spikes. The spikes in the layers can lead to shorts. These shorts here result from the vertical conform layer formation of Alq3.[83]

6.5 Discussion on silver grids

The proof of concept that inkjet printed grids can replace ITO as transparent electrode was shown in this chapter. Different grid dimensions were tested to check the influence on an OLED device. Table 1 shows the figure of merit of the presented devices and sums up the important data. Overall the coverage decreases with increasing spacing size, except for identical spacings with different line thicknesses. The onset for this material and this layer thickness is independent of the grid dimension as all devices showed the same onset voltage of approximately 3.6 V. All devices suffer a comparable degradation related to PSS. The devices displayed a low current density in reverse bias down to 5 V. The devices with the grid spacing of 3 mm and a line width of 150 µm and the spacing of 5 mm and width 150 µm showed the most promising performances.

Table 1: Summary of structure and performance of PLEDs; the coverage is the area covered by grid lines divided by the total area of the grid times one hundred

Grid dimensions: s [mm] x w [µm]	**Max. Efficency [cd/A]**	**Efficency[a] at [cd/A]**	**luminance [cd/m^2]**	**Coverage [%]**
1.5 x 90	3.8	3.7	12000	21.4
2 x 90	3.5	3.0	14500	26.9
3 x 90	2.3	2.3	5000	21.7
3 x 150	7.0	5.2	45000	24.5
5 x 150 extra busbar	6.0	3.5	40000	16.3
5 x 150	5.5	4.2	47000	16.3
8 x 150	9.4	7.0	26000	11.7

a) At 1000 cd/m^2

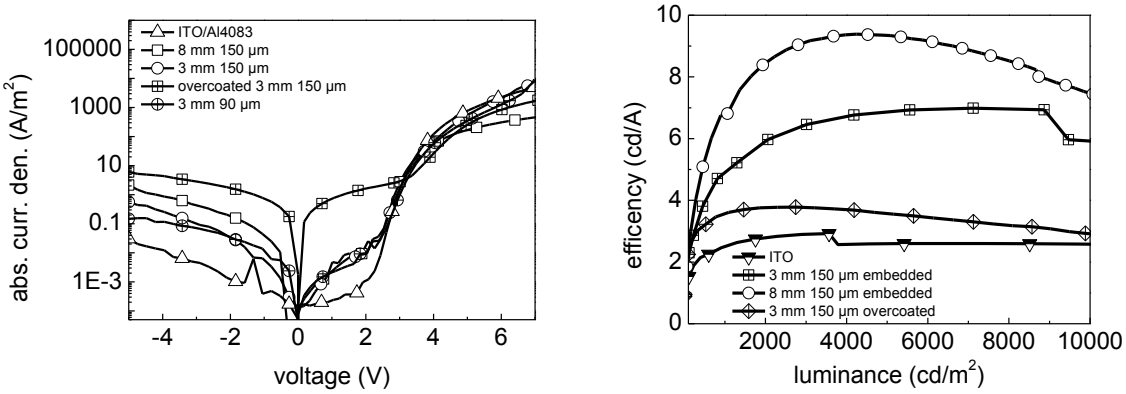

Figure 41: Left: Logarithmic plot of current density versus voltage of various embedded grid structures, over coated grids and ITO devices. Right: Efficiency plotted over luminance of embedded and overcoated grids, further devices with ITO anode.

On the left of Figure 41 the absolute current density of 3 different embedded and an overcoated grid structures and further an ITO device are plotted. For a good working OLED the values under backward bias should as low as possible to state few shorts and enhance the possibility of a high efficency. Lowest cut-off current is achieved by the ITO device. Embedded grids show, depending on the dimension higher cut-off currents from 0.1 – 8.0 A/m^2. The overcoated grid exhibit the highest cut-off current of 10 A/m^2. Under forward bias the ITO device keeps the lowest cut-off current up to 3.6 V. At 3.6 V all devices switch on. In the forward bias regime the difference between embedded and overcoated grids becomes significant. The cut-off current is almost 3 magnitudes higher.

Figure 41 to the right comprise the efficiency plotted over the luminance. Again PLEDs on embedded and over coated grids and ITO are plotted. While the ITO device features low turn-off currents it has the lowest efficiency in the range from 0 to 10000 cd/m^2 operating emission. The over coated grid although exhibiting a high turn-off current have an average efficiency of approximately 3.8 cd/A. The embedded grid structures reach depending on the dimension up to 9.4 cd/A.

7 Copper ink

Additionally to silver ink, copper ink was used to print grids. In general inkjet printed copper grids are favourable to silver ink due to the lower material costs. The here presented data is in the same order as in chapter 6. At the beginning over coated grids and their performances are presented, followed by embedded grids. For the two parts of the experiments the two different inks as described in 4.1 were used.

7.1 Inkjet printed overcoated copper grids with solution processed HIL and LEP

For the first overcoated experiments the Intrinsiq 005G ink was used. It turned out to be a adheasion optimized ink. Hence it was impossible to perform the embedding and lift-off process. Further these grids were sintered in a special reactor under formic acid atmosphere. It was expected that this kind of sintering leads to a homogeneous and less rough surface compared to usually laser sintered inkjet printed lines further these lines should exhibit a better conductivity. This benefits should make the embedding process unnecessary for a good performance. As explained in 4.1. Following are described the difference influences of different sintering temperatures and the devices with the most promising copper grids.

7.1.1 Copper grids sintered at 180°C in formic acid

The grid dimensions were equal as for the Ag grids. Figure 42 comprises 3 microscope pictures of a copper grid sintered in formic acid at 180°C. Grid parameters are 1.5 mm hexagon spacing and 90 µm line width. Figure 42 a shows the hexagons in a closer look. The ink is trickled during the printing process and no exact hexagons are left. Figure 42 b displays one grid line with a larger magnification. From the center of the line to the edge (left to right) the line height seems to increase and peak at the edge. Figure 42 c confirms this increase in height as it is a dark mode picture. In dark mode obstacles which are out of plane are enlightened. The increase in height at the edge of the inkjet printed line is due to the coffee ring effect. [84]

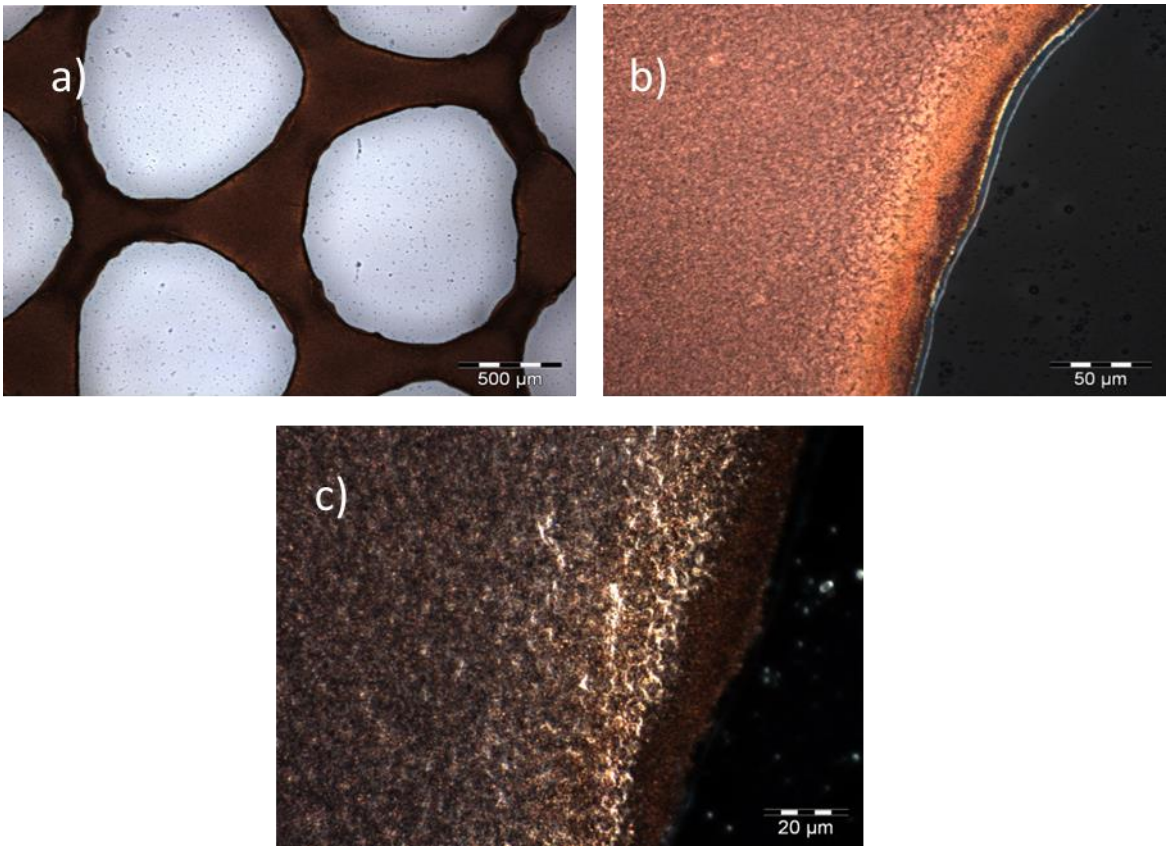

Figure 42: a) Optical microscope picture of the a copper grid with 1.5 mm spacing and 90 µm line width. b) Shows the same grid with bigger magnification at the edege. c) Displays the same grid with a magnification (100 x) in dark mode.

7.1.2 Copper grids sintered at 200 °C in formic acid

These grids were sintered at 200 °C and had the lowest resistivity of only 5 Ohm measured from bus bar to bus bar. As the ink was the same as the previous one we again see the ink has trickled away during printing and the hexagons transformed to circle like structures (Figure 43 a). According to this fact, it is for sure an ink property and no sintering issue. The difference in sintering temperature becomes clear with a closer look on the microscope pictures. Figure 43 b show dark spots in the normal mode microscope picture. Dark mode picture (Figure 43 c) confirm that these are not holes, but structures standing out of the plane.

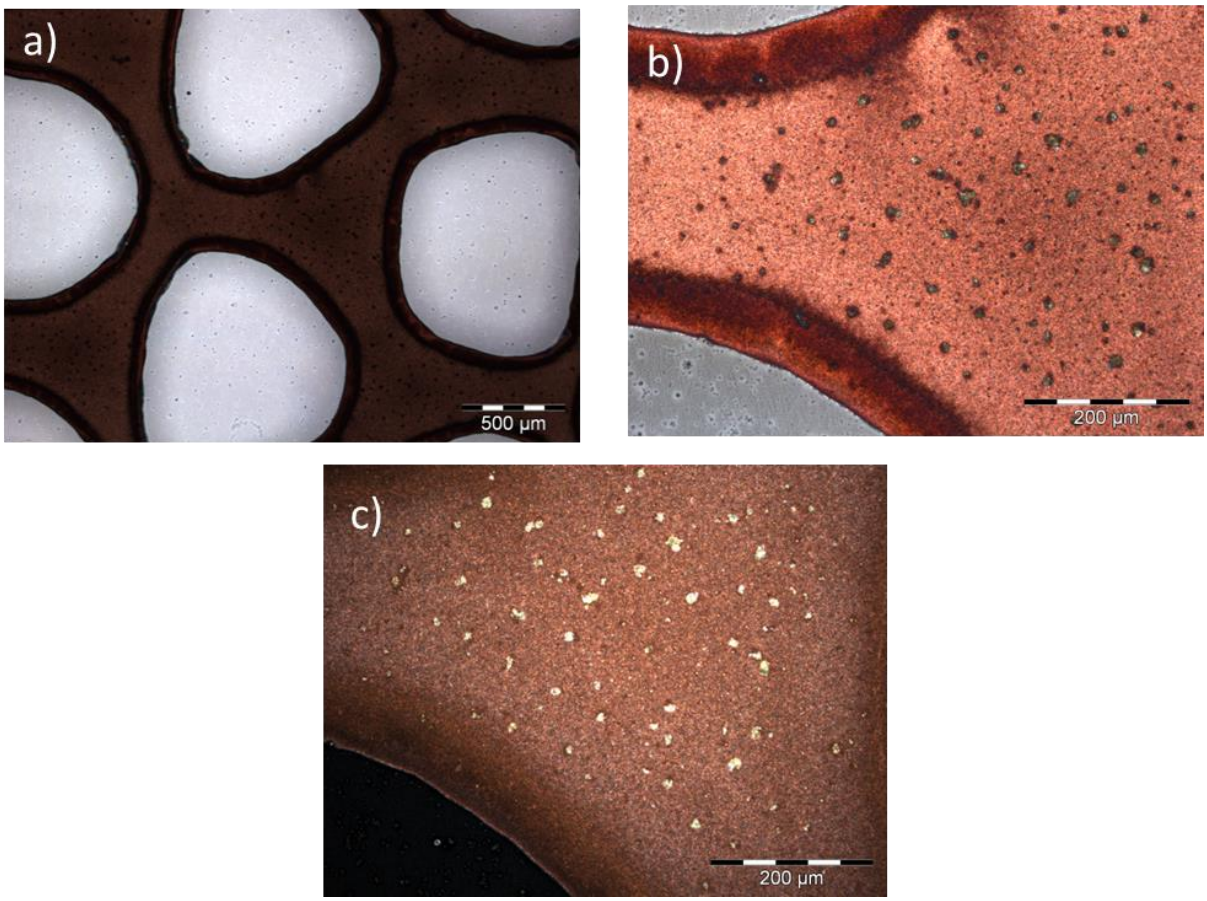

Figure 43: Copper grid with 1.5 mm spacing and 90 µm line wideth sintered at 200°C; a) Microscope picture of the grid. b) Line in more detail, the line height is clearly visible at the edges of the line. c) Dark mode picture of b to compare the dark spots.

These grids showed the highest conductivity hence they were choosen for OLED processing. The various dimensions and performance details are presented in the following parts. Due to comparability the same solutions were processed PLEDs were processed on the grids as in chapter 6. The same processes and materials were applied here.

Grids with 2 mm spacing and 90 µm width

The first investigated grid sintered at 200°C had 2 mm spacing and 90 µm line width. The PLED stack is the same as in chapter 6. Figure 44 shows the current-photocurrent characteristics. Due to low device yield and fast failure it was impossible to calibrate the photo diode properly. The photocurrent is an approximate indicator for brightness. The photocurrent is increasing similar to luminance in former devices. The cut-off current at -5 V is 0.4 mA indicating a low shunt resistance. As visible in Figure 45 the not the same area as the cathode was emitting light therefor it was impossible to calculate a current density.

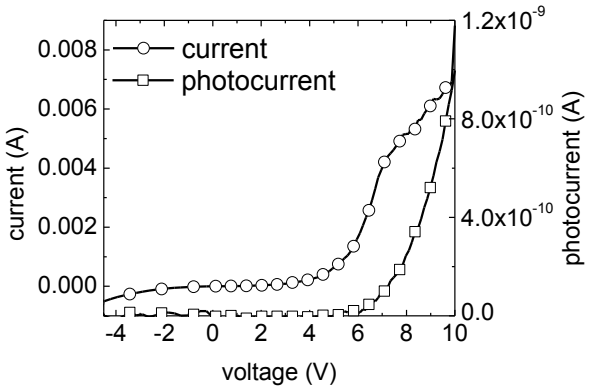

Figure 44: Current-photocurrent characteristics of solution processed PLEDs on copper grids sintered in formic acid at 200°C.

Figure 45 shows a picture of the described PLED on the copper grid. Strong inohomogenities in light emission are visible.

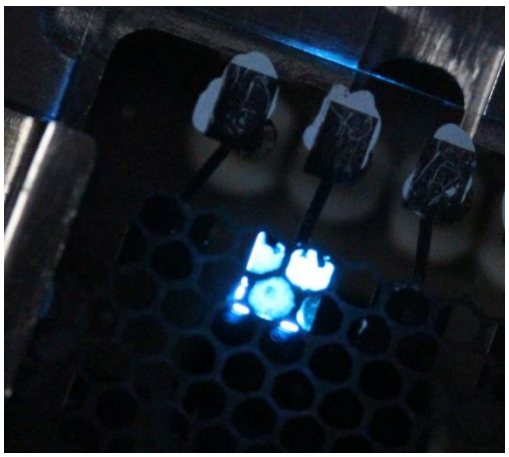

Figure 45: Working PLED on over coated copper grid, the luminescent area shows many failures.

Grids with 3 mm spacing and 150 µm line width

These grids were made as the previous except the F CE PEDOT:PSS layer was approximately 200 nm instead of 150 nm. The thicker PEDOT:PSS layer was choosen to reduce shorts which occurred in the previous experiment. Figure 46 (left) shows the voltage-current-luminance characteristics of this device. The cut-off current density of 890 A/m^2 indicates a again many shorts through the layers. A maximum current density of 15000 A/m^2 was reached. The current density characteristics are very noisy compared to other devices. Also the luminance characteristics are noisy and reaches a maximum value of 4800 cd/m^2. The onset is at 3.6 V.

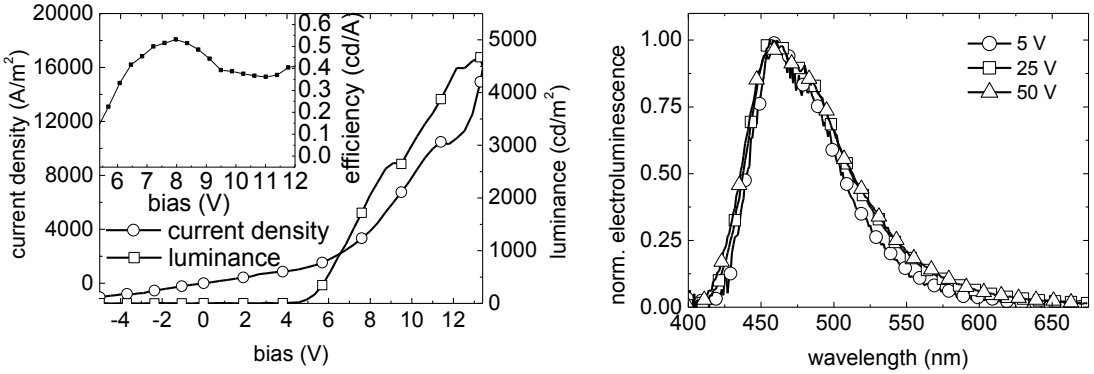

Figure 46: Left: Current-voltage-luminance characteristics of a PLED on a overcoated copper grid with 3 mm spacing and 150 µm line width. Right: Electroluminescence spectra of PLEDs on overcoated copper grids.

Figure 46 (right) are the electroluminescence spectra at various voltages. This device seems to be more stable as almost no peak shift is visible. Figure 47 shows a PLED on an over coated copper grid with increasing driving voltage from a to c. At low operating voltages (a) the inohmogenity in the electric field and subsequent the luminance becomes clearly visible. The closer to the grid line the higher the luminance. Even at higher operating voltages (b) the inhomogeneity is visible. The inhomogeneity seems to vanish at operating voltages above 12 V (c). Figure 46 (c) also shows the bright and blue emission of the material. Further the grid structure seems to vanish for the naked eye because of the high brightness. Because of the thermal curing of the HIL and the LEP layer cracks occurred in some Ormocomp layers.

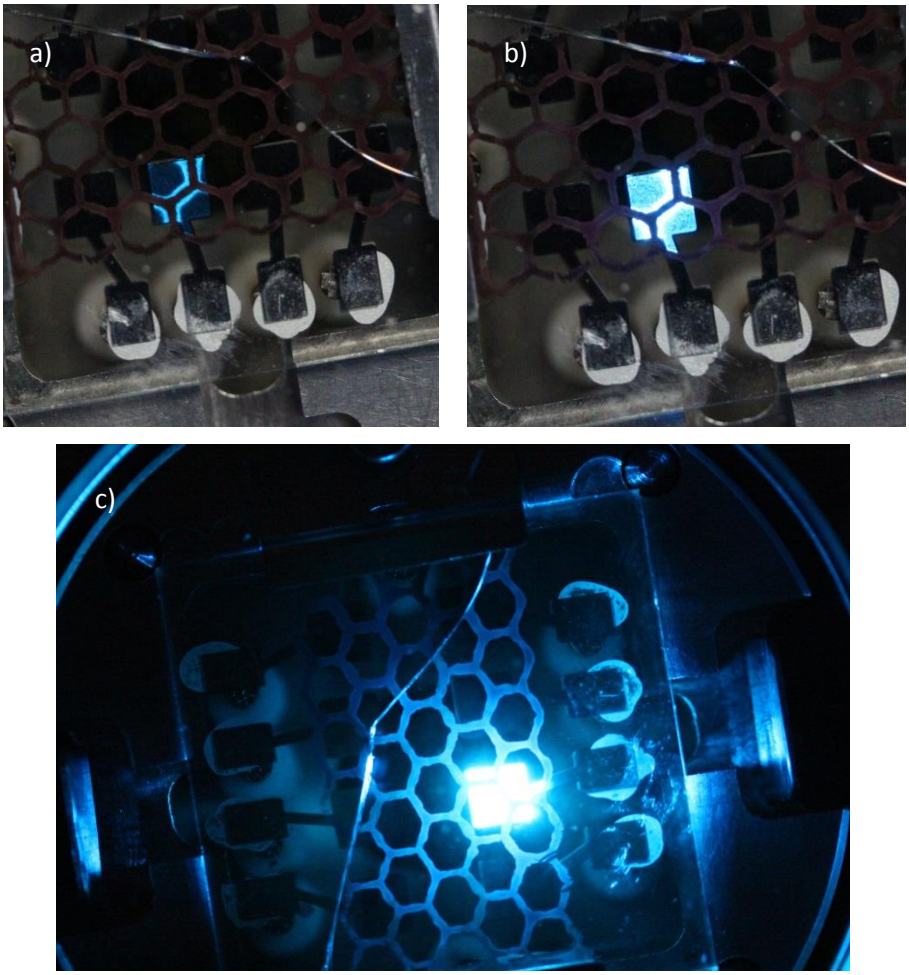

Figure 47: PLEDs on overcoated copper grids at varous driving voltages.

Grids with 5 mm spacing and 150 µm width

These grids were again covered with a 150 nm layer F CE PEDOT before depositing the usual PLED layers. The calibration of the photodiode was impossible due to low device yield and fast failure. Due to shorts were the active areas of the OLEDs undefined. Therefor there are neither current density nor the luminance are in the characteristics, but the current and the photocurrent. Although the device yield was low the characteristics in Figure 48 is smooth. An ohmic behaviour in forward bias is visible as the current increases linear from 0 V to 4 V.

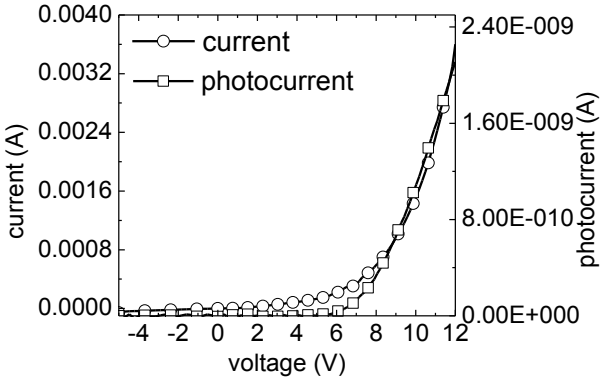

Figure 48: Current photocurrent characteristics of PLED on over coated copper grids with 5 mm spacing and 150 µm line width.

Figure 49 shows on PLED of this device under operation. Inhomogeneity of the emissive area is visible causing an undefined active area of the device. Additionally the device is split in electroluminescence because of the grid line.

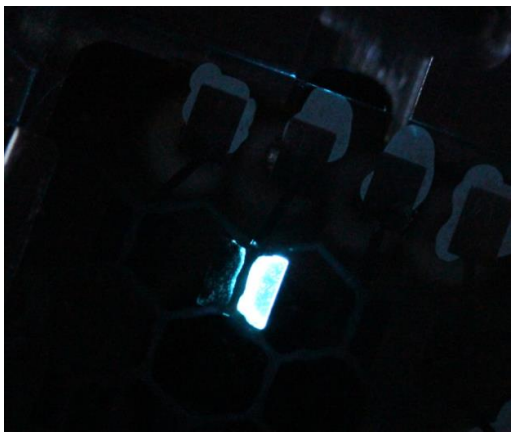

Figure 49: PLED on over coated copper grid with 5 mm grid spacing and 150 µm line width during operation.

Grids with 8 mm spacing and 150 µm line width

For this grid the PEDOT:PSS F CE layer was increased to 200 nm as previous experiments showed that a thicker layer of PEDOT:PSS is necessary for a better overcoating and thus a higher device yield. Further PLED layers were deposited equally to the previous.

Figure 50 displays the results of the PLEDs on overcoated copper grids with a spacing of 8 mm and a line width of 150 µm. Due to the thicker PEDOT:PSS layer a fully characterisation with calibration of the photodiode was possible. Current density reached its maximum at 3000 A/m^2. Luminance peaked at 2800 cd/m^2. From this values a maximum efficiency of 1.0 cd/A and an efficiency at 1000 cd/m^2 of 1.0 cd/A was calculated (see inset Figure 50). The thicker PEDOT:PSS layer may have increased device yield and made a full characterisation possible. However the drawback is an increased serial

resistance in the OLED stack. Due to this fact luminance and current density increase almost linear, with increasing voltage from 3.6 V on. Further the efficiency did not reach 9.0 cd/A as compared to the silver grid.

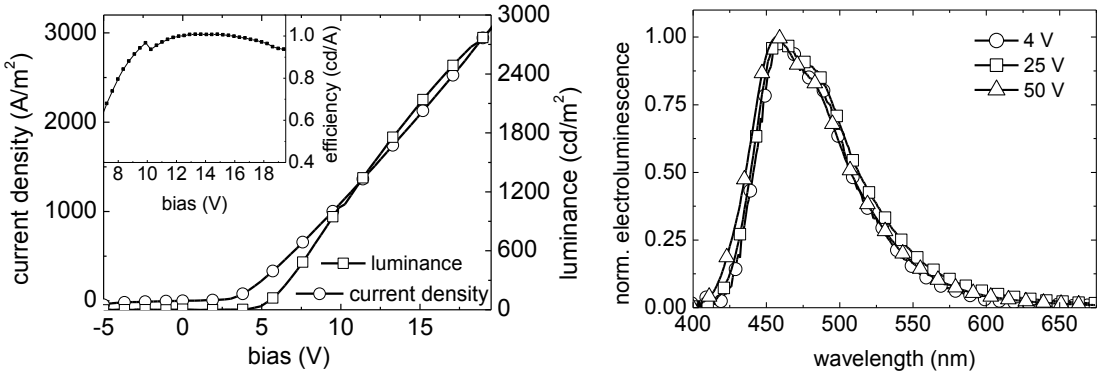

Figure 50: Left: Current-voltage-luminance characteristics of a PLED on an overcoated copper grid with 8 mm spacing and 150 µm line width. Right: According electroluminescence spectra of PLEDs on overcoated copper grids.

Figure 51 (right) presents the electroluminescence spectrum of the described device. It remained stable over the voltage sweep from 4 V to 10 V.

Although the serial resistance is large due to the PEDOT layer of 200 nm, pictures with high brightness were taken. Figure 51 displays the described PLED under operation. The high brightness was achieved via applying high voltages (up to 20 V). Still the device did not show significant degradation, as noticeable from the bright and blue emitted light. Although the cathode is mostly surrounded by the hexagon a homogeneous emission was achieved.

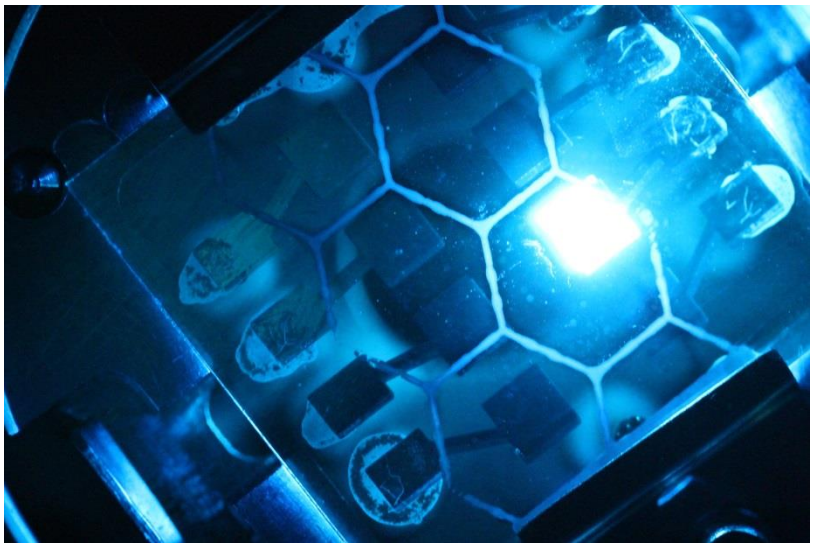

Figure 51: PLED on overcoated copper grid with 8 mm spacing and 150 µm.

7.1.3 Copper grids sintered at 250 °C in formic acid

These grids were sintered at 250 °C and showed a resistivity of 266 Ω measured from bus bar to bus bar. The serial resistance would have been too high to process efficient OLEDs on them. Figure 52 shows microscope pictures of a grid with 1.5 mm line spacing and a line width of 90 µm. Figure 52 a shows an overview in dark mode over the hexagons with the same magnification as in Figure 42 a and Figure 43 a. The hexagons are circle like structures due to trickling of the ink while printing. Cracks are at this magnification. In dark mode, a different surface structure visible compared to Figure 42 a and Figure 43 a was found. Figure 52 b gives a closer look on the line. Compared with Figure 43 b crystallite like structures are visible. Additionally to the crystallites large black areas occur which seem to be destroyed and missing ink parts. Figure 52 gives a closer look on one of the crystallites. With the highest magnification (100 x) cracks in the crystallite are already visible.

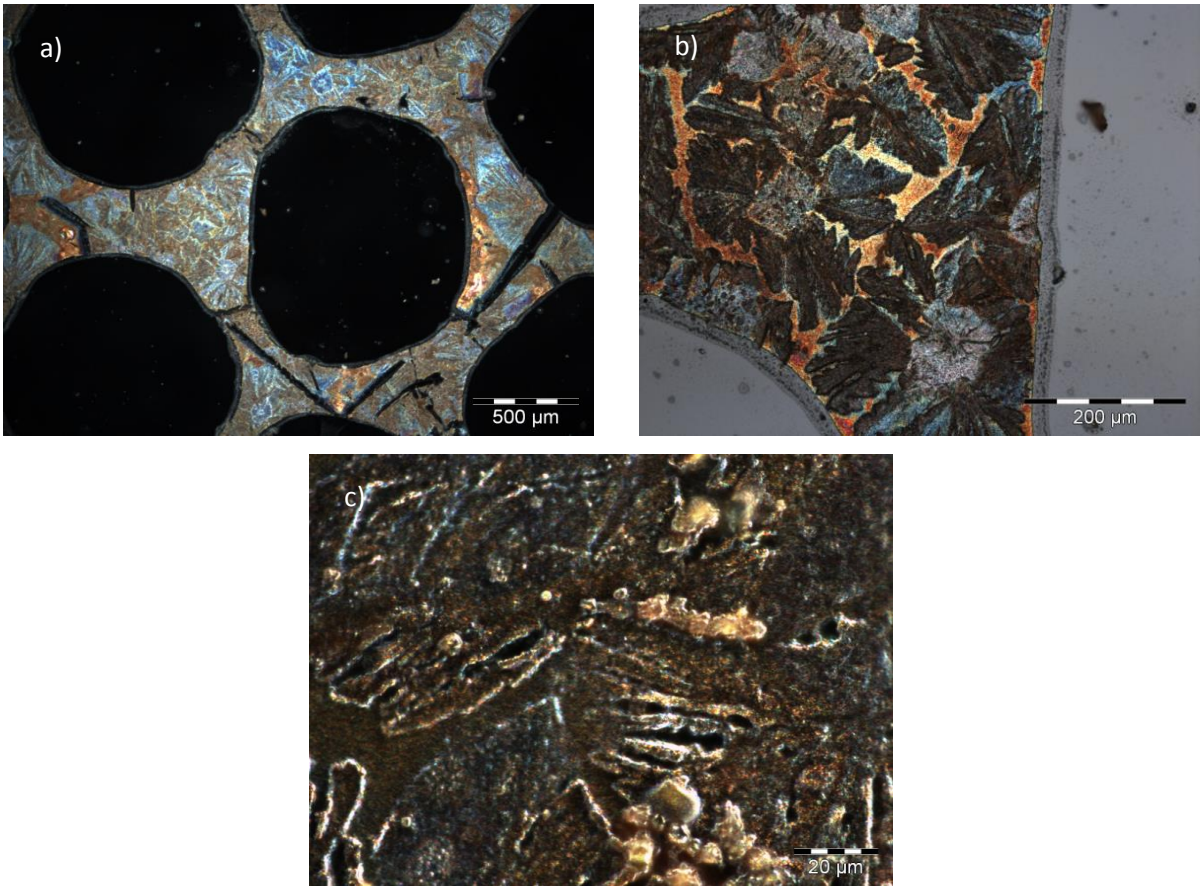

Figure 52: microscope pictures of copper grids sintered in formic acid a-c increasing magnification.

7.2 Inkjet printed embedded copper grids with solution processed HIL and LEP

First experiments with the copper ink 005G showed that embedding and lift off was impossible with this ink due to improved adhesion. For embedding experiments the intrinsiq 003G ink was used. With this ink the embedding process was applicable the same way as for silver inks. For the here presented devices the same materials and methods as in chapter 6 were used. The following parts describe the performances of embedded copper grids with various dimensions as transparent conductive electrodes for PLEDs.

Embedded copper grid with 1.5 mm spacing and 90 µm line width

Figure 53 presents the current density – luminance characteristics of the smallest grid with 1.5 mm spacing and 90 µm line width. Although the grid was embedded the characteristics show ohmic behaviour. From -5 V to 9 V the current density increases linear. A maximum current density of 900 A/m^2 was reached. The maximum luminance was 120 cd/m^2. The electroluminscence spectrum is stable up to 14 V operating voltage.

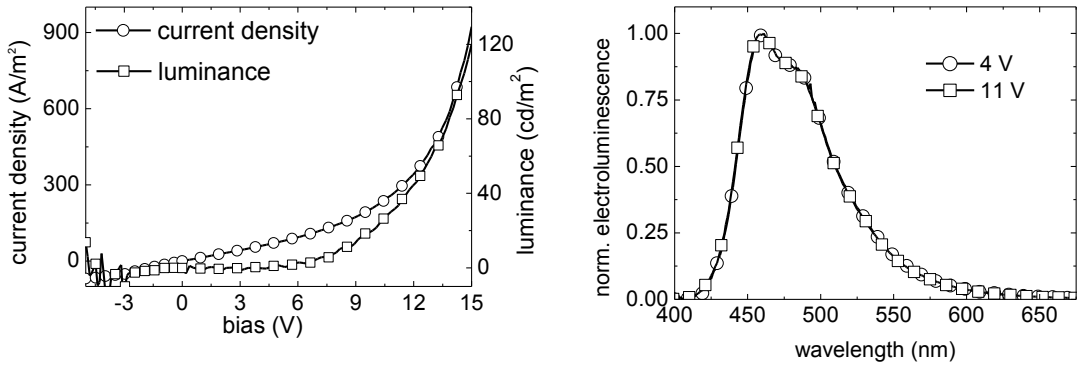

Figure 53: Left: Current density and luminance of PLEDs on embedded copper grids with 1.5 mm spacing and 90 µm line width. Right: According electroluminescence specrtrum.

Figure 54 shows the described PLED under operation. Bright and blue light emission was achieved, although the shorts. Although an operating voltage of 17 V and a line width of 90 µm the grid lines are still visible.

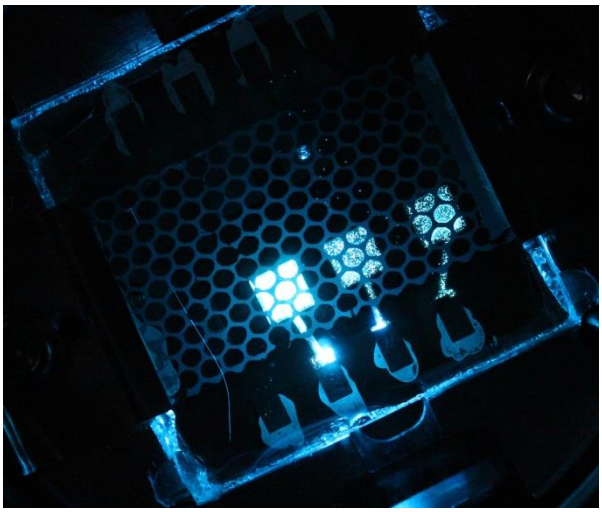

Figure 54: PLED on embedded inkjet printed copper grid with 1.5 mm line spacing and 90 µm line width.

Embedded copper grid with 2 mm line spacing and 90 µm line width

No I-V-luminance data were measured as the device failed too fast. Figure 55 displays the electroluminescence spectrum. The spectrum confirms the fast degradation. At 9 V the first spectrum was measured and it shows already a peak shift to the red from 451 nm to 488 nm.

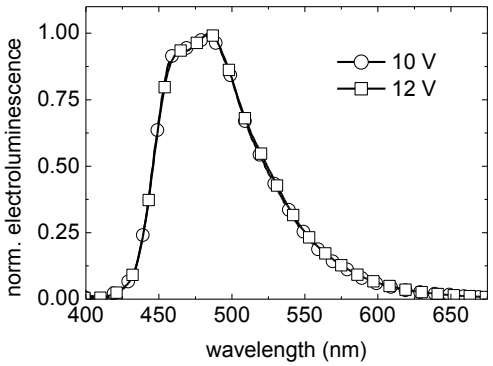

Figure 55: Electroluminescence spectrum of PLED on an embedded copper grid with 2 mm line spacing and 90 µm lien width.

At lower operating voltage, it was impossible to measure any spectra, because the luminance was to low. Figure 56 shows a picture of the PLED under operation. The emissive area is inhomogeneous. Due to the low operating voltage the grid lines are clearly visible.

Figure 56: Operating PLED on an embedded copper grid with 2 mm line spacing and 90 µm line width.

Embedded copper grid with spacing 3 mm and line width 150 µm

The grid with 3 mm line spacing and 150 µm line width is the biggest embedded copper grid structure presented. Figure 57 shows the current density and the luminance characteristics of the grid. Additionally to the linear increase in current density from -3 V to 6 V the line shows a noisy behaviour. The maximum current density was determined to be 320 A/m^2. Maximum luminance value was measured at 220 cd/m^2. A short loss in luminance is visible at 9 V. Overall the device did not feature a stable operation. Caused by this low luminance, electroluminescence spectra were only measured at 7 V and 12 V. Figure 57 to right shows this spectra. Again the peaks are already red shifted from 451 nm to 488 nm due to the keto defect.

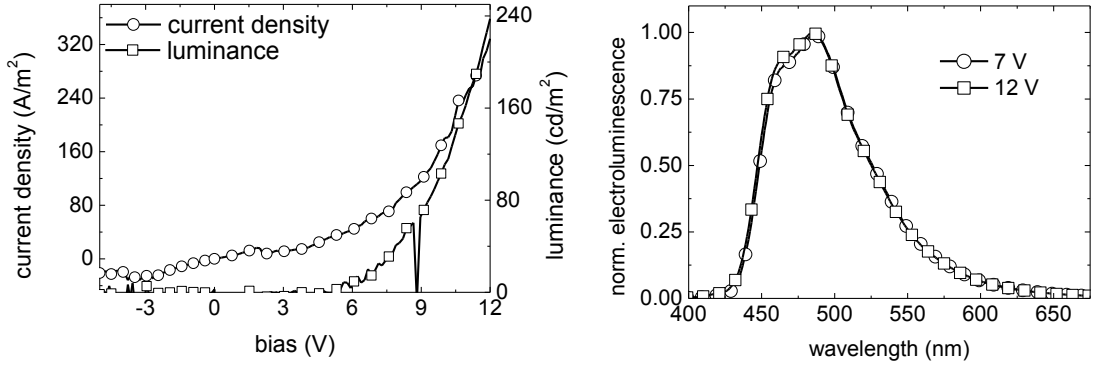

Figure 57: Left: Voltage-current-luminance luminance characteristics of a PLED on an embedded copper grid with 3 mm line spacing and 150 µm line width. Right: According electroluminescence spectra.

Figure 58 displays the described PLED on the embedded copper grid under operation. A bright blue emission was achieved by applying 17 V. The dark spot next to the PLED under operation is an air bubble. The air bubble derives from the embedding process. From the air bubble cracks through the PLED layers occurred.

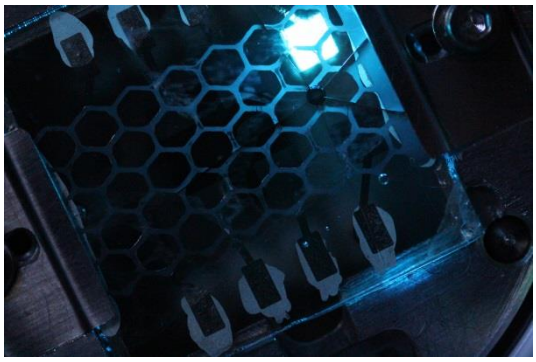

Figure 58: PLED on embedded copper grid with 3 mm spacing and 150 µm line width.

7.3 Discussion on copper grids

The first part of the here presented copper grids were overcoated and used the 005G copper ink sintered in formic acid. The second part presented embedded copper grids which were printed with intrinsiq 003G ink and laser sintered. Due to these differences it is impossible to link different performances to embedding or overcoating. In contrast to the silver grids the overcoated copper grids seemed to perform better. The over coated grids reached efficiencies up to 1.0 cd/A (8 mm spacing, 150 µm line width). Overall the inkjet printed copper grids perform worse than the inkjet printed silver grids. Table 2 sums up the main facts of the copper grids.

Table 2: Comparison of over-coated and embedded copper grids

Grid dimensions s [mm] x w [µm]	**Max. Efficency [cd/A]**	**Efficency [cd/A]**[a)]	**Max. luminance [cd/A]**	**Coverage [%]**
8 x 150 overcoated	1.0	1.0	2800	11.7
3 x 150 embedded	-	-	240	24.5

a) Measured at 1000 cd/m^2

8 Ag nanowires as transparent conductive electrodes

As alternative to inkjet printed grids highly disordered micro grids were tested. Silver nanowire networks were first investigated as transparent conductive electrodes by Lee et al.[61]. This chapter deals with the fabrication and characterisation of nanowire thin films. Further solution processed PLEDs and thermal evaporated OLEDs on Ag nanowire thin films are presented. The nanowires used for this thesis were delivered by Sigma Aldrich. They came in a solution of 0.5 wt% in isopropyl alcohol suspension.

8.1 Characterization of Ag nanowires

Before starting to use nanowire thin films as transparent conductive electrodes various ways of depositing the film were tested. The here presented thin films were spincasted with 3000 rpm for 1 second. The short spinning time is necessary to avoid radial inhomogenities due to agglomerates moving from the center to the edge. Subsequent to spincasting the films were annealed for 20 min at 180°C.

SEM and AFM pictures

Figure 59 a shows a SEM image of this layer. The wires form highly disordered micromesh like structures. To study the different coverage conditions the pure solution from Sigma Aldrich was further diluted. Figure 59 b displays a layer of 75% nanowire solution in isopropanol. It illustrates a lower concentration of nanowires. Also agglomerates of nanowires become less with lesser concentration. Figure 59 c and Figure 59 d show SEM images of even further diluted (50% and 25%) nanowire layers. Figure 60 shows an AFM picture of a 75% diluted nano wire thin film. In contrast to the SEM pictures a stronger surface roughness impression is visible. On the 10 µm times 10 µm measured section spikes with heights up to 150 nm are visible.

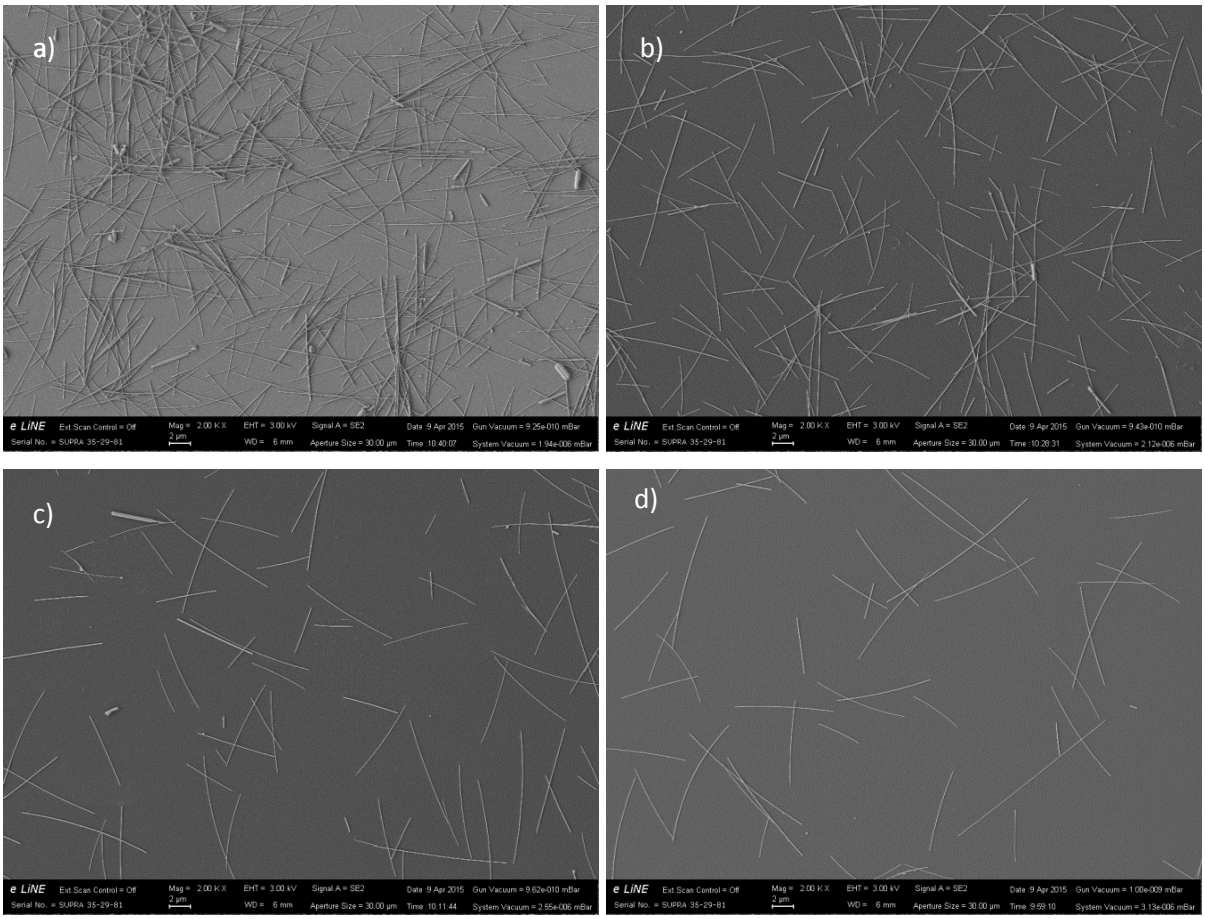

Figure 59: a) Pure silver nanowire solution spincoated. b) 75% dilutetd silver nanowire solution spincoated. c) 50% diluted silver nanowire solution spincoated. d) 25% diluted silver nanowires spincoated.

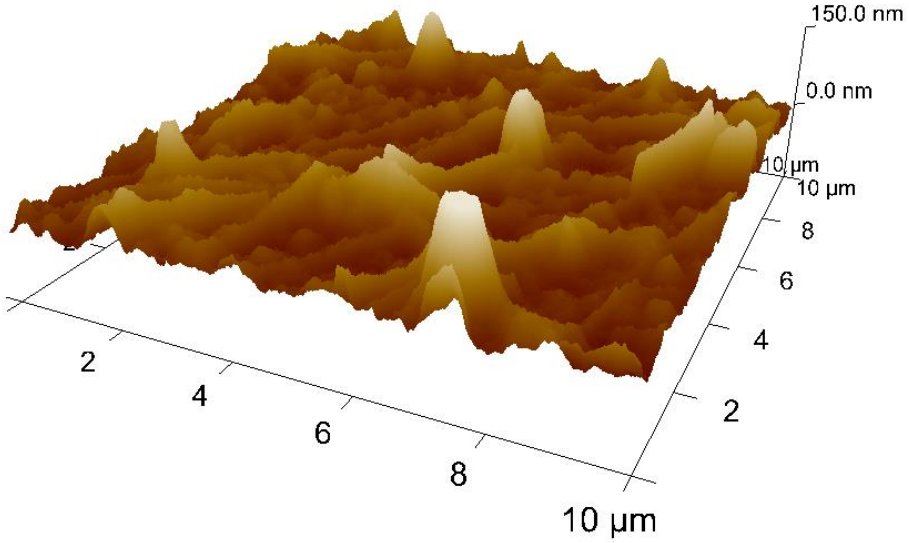

Figure 60: AFM picture of a nano wire thin film, spikes with heights up to 150 nm are visible.

Transmission measurements of various silver nanowire films

According to the SEM Images transmission measurements of the nanowire films were performed. Therefor the same PerkinElmar 900 UV/VIS as for the silver grid specification was used. All samples from the SEM measurements were measured. The transmission spectra in Figure 61 confirm the SEM measurements. The film made of the pure solution from Sigma Aldrich (circle with cross) exhibits the lowest transmission in total (68% - 70% depending of the wavelength). With a concentration of 75% nanowires an average transmission of 85% was measured (squares with cross). The transmission of the films with 50% (open circles) and 25% (open squares) lay close together at 93% to 95% depending on the wave length. The higher the nanowire concentration the lower the transmission.

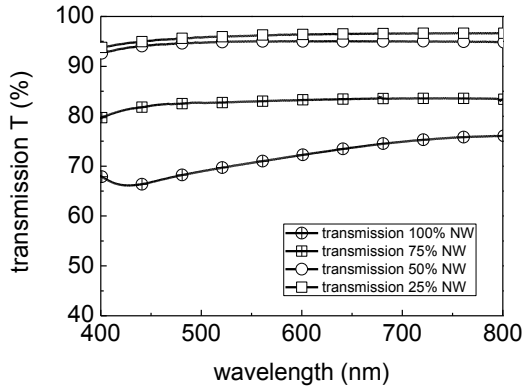

Figure 61: Transmission of thin film layers of various diluted nanowire solutions.

8.2 Device performance

Based on the investigations of the nanowire thin films in 8.1 a concentration of 60% nanowires was choosen. On the basis of this concentration the transparent conductive electrodes were fabricated as described in the following part. Solution processed PLEDs and thermally evaporated OLEDs were processed on this films equally to chapter 6.

Device fabrication

The pure nanowires exhibited rough surface structure as shown in the SEM and AFM pictures. To overcome this issue and get a smoother electrode surface the wires were mixed with PEDOT:PSS. The idea is that the PEDOT:PSS forms a layer in which the nanowires are embedded. Further Nanowires show a large contact resistance were they lay on each other. [61] Work by Kim et al. showed that a

combination of nanowires and PEDOT:PSS in solution enhances the conductivity.[60] The nanowires were first mixed with various concentrations in PEDOT. The original silver nanowire solution from Sigma Aldrich was diluted with PEDOT to obtain 60% nanowire solution in PEDOT:PSS. This solutions were then spincoated and heated for 20 minutes at 180 °C. Baking of the films was necessary to minimize the contact resist of the nanowires. [61] On this transparent anode 2 additional layer of PEDOT were added.

Device Characteristics of evaporated Alq3 and NPB devices on nanowire thin film electrodes

These first devices were made with thermal evaporated Alq3 and NPB. Figure 62 reveals the problems of nanowires as transparent conductive electrodes. The current density in backward bias reaches almost 1000 A/m^2. This is an indicator for shorts. Further the current density in forward bias increases almost linear. The maximum luminance of this device is 500 cd/m^2, at a bias of 20 V. This is too high for a reasonable operation of an OLED. The luminance from 0 V to 15 V can be referred as noise, from this follows the low maximum efficiency of 0.25 cd/A (inset in Figure 62).

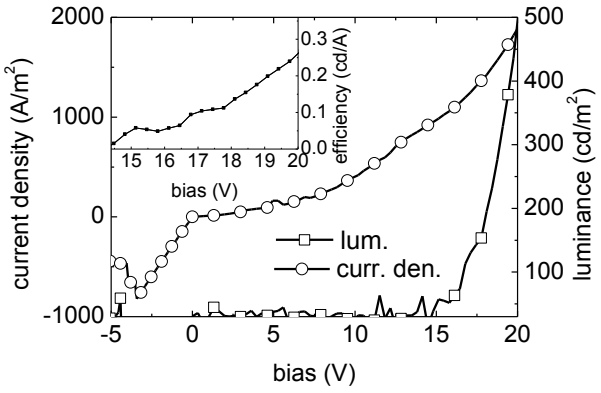

Figure 62: Voltage-current-luminance characteristics of evaporated OLED on AgNW/PEDOT solution

Although measuring the emission spectra was impossible Figure 63 shows a working device. In this figure no shadowing is obtained at all, which is comparable to ITO. The green emission is typical for Alq3. Figure 63 (right) shows the same panel a few minutes later. One can see a colour change.

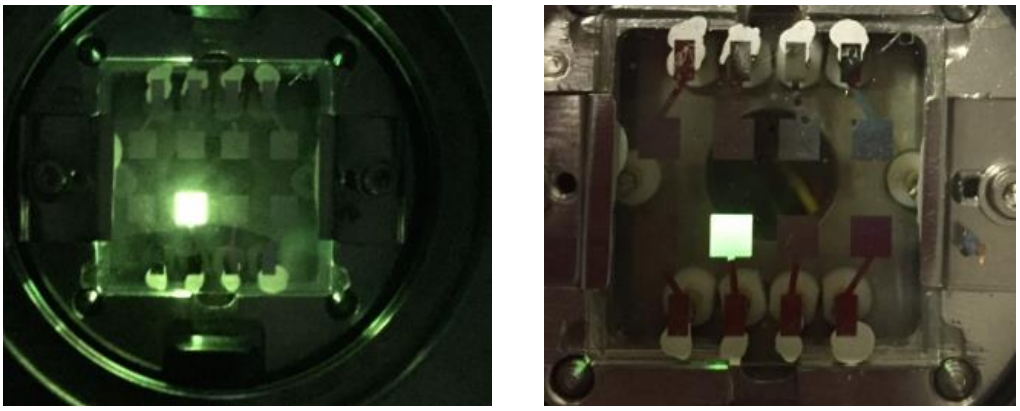

Figure 63: Operating Alq3 OLED on AgNW (left) and degraded Alq3 on AgNW (right).

Device Characteristics of Solution processed OLEDs

The solution processed OLEDs on PEDOT/NW mixtures were processed with the same CPs as the solution processed on the grids. The solution processed OLEDs on the silver nanowires did not work at all. Most devices showed shorts and therefore ohmic behaviour in the characteristics. Further they emitted only light at the edges of the Cathodes before they got short circuited because of defects.

8.3 Discussion on silver nanowires

In contrast to previous observations on the inkjet printed grids, solution processed OLEDs on nanowires performed far worse than the evaporated. The reason for this behaviour is unclear so far. Nano wire networks comprise sufficient conductivity for the use in OLEDs. The major benefit of nano wires is the homogeneity of the electrode, as shown by Figure 63. No field dependent luminescence inhomogenities are visible compared to the grids. Further is a significant shadowing excluded. Shortcuts due to the rough surface are still the major problem for achieving higher efficiencies. To apply nano wires as TCEs this issue needs to be solved.

9 Conclusion

The scope of this thesis was the investigation of transparent conductive electrodes in order to find a viable replacement for ITO. In this context, different materials and layouts have been evaluated. They can basically be subdivided into

- Electrodes based on inkjet printed silver
- Electrodes based on inkjet printed copper
- Electrodes based on a silver nanowires random microgrid.

Chapter 4 explains all applied methods and experimental details including the process of inkjet printing. A printed honeycomb layout was chosen in order to minimize coverage and the resulting unfavourable shadowing during light out coupling. The printed grids were varied with respect to their size/diameter in order to find the optimum trade-off between shadowing and conductivity.
Chapter 5 presents a conventional OLED using an ITO electrode which is further used as a reference device for comparison.
Chapter 6 deals with inkjet printed silver electrodes. It was demonstrated that grids with a relatively high coverage (~ 25%) already show a comparable transmission to ITO. All grids with a larger diameter are naturally better in transmission compared to ITO. The first set of OLEDs was fabricated by simply overcoating the electodes with the functional layers required for an OLED. High conductive and high viscosity PEDOT:PSS (Clevious F CE) was used to guarantee a low voltage drop in the areas in-between the grid lines as well as a suitable overcoating of the rough and high grid lines. This resulted in efficiencies and luminance values of 3.4 cd/A and 19000 cd/m^2, respectively, which is already comparable to the ITO device. To overcome the issue that there are significant defects present in these devices, the electrodes were embedded/planarized (for details of the embedding process see chapter 4.2) in a second step. Embedding indeed reduced the contribution of shunt current by several orders of magnitude while the efficiency of the best performing device was increased to 9.4 cd/A. This corresponds to an increase of 250 % as compared to the ITO reference device. The electroluminescence spectra of the PLEDs employing grid electrodes remained stable during the measured voltage sweeps and no significant shift was visible.

Additionally to the solution processed PLEDs thermal evaporated OLEDs are presented in chapter 6.4. Due to the here unfavourable film formation properties of small molecules, these OLEDs displayed

ohmic behaviour in the IV-characteristics. From this it can be concluded that for rough and high grid electrodes a solution processing is superior.

Chapter 7 presents copper ink based grids. Motivated from the successful implementation of silver grids, the same structures were tested with copper ink. Here, two different inks with different properties and sintering procedures were applied. First, formic acid sintering was used giving conductive structures for defined processing conditions. An embedding process was however not possible due to high adhesion of the printed and sintered ink on the sacrificial substrate. Therefore a second ink with lower adhesion was sintered using a IR laser and further on used for the embedding process. Both procedures gave working devices, their performance however did not reach the values of the ITO based reference device. The maximum efficiencies were 1.0 cd/A (overcoated) and the luminance was 2800 cd/m^2.

In chapter 8 silver nanowires as highly disordered micro grids in thin films were tested. The nanowires were mixed with PEDOT and thin films were fabricated on glass substrates. On this thin films thermal evaporated OLEDs were processed. The devices showed ohmic behaviour due to the random orientation of the nanowires and delivered efficiencies of 0.3 cd/A.

Table 2 summarizes the figures-of-merit of the most important devices structures.

Table 3: Summarizing the most important grid structures and their performance

Grid structure s [mm] x w [µm]	**Max. Efficency [cd/A]**	**Efficency [cd/A]**[a)]	**Max. luminance [cd/A]**	**Coverage [%]**
ITO	3.7	2.8	60000	0
3 x 150 overcoated	3.4	3.1	19000	24.5
3 x 150 embedded	7.0	5.2	45000	24.5
8 x 150 embedded	9.4	7.0	26000	11.7
Copper grid 8 x 150 overcoated	1.0	1.0	2800	11.7

a) Measured at 1000 cd/m^2

So far, inkjet printed silver grids exceed ITO as transparent conductive electrodes in efficiency. With the applied embedding and flip over process a further increase in efficiency compared to over coated grids was achieved. The cut-off current was lowered 3 orders of magnitude compared to over coated grids. The stability of the emission spectra was independent of the grids. Printed copper grids also gave working devices, their performance, however, did not reach the values of ITO based devices.
The content of this work shows that inkjet printed anode setups are a serious low-cost competitor to established technologies.

10 Bibliography

[1] W. Ma, C. Yang, X. Gong, K. Lee, and A. J. Heeger, “Thermally Stable, Efficient Polymer Solar Cells with Nanoscale Control of the Interpenetrating Network Morphology,” *Adv. Funct. Mater.*, vol. 15, no. 10, pp. 1617–1622, 2005.

[2] C. G. Granqvist, “Transparent conductors as solar energy materials: A panoramic review,” *Sol. Energy Mater. Sol. Cells*, vol. 91, no. 17, pp. 1529–1598, 2007.

[3] T. C. Hales, “The Honeycomb Problem on the Sphere,” pp. 1–18, 2002.

[4] I. Burgués-Ceballos, N. Kehagias, C. M. Sotomayor-Torres, M. Campoy-Quiles, and P. D. Lacharmoise, “Embedded inkjet printed silver grids for ITO-free organic solar cells with high fill factor,” *Sol. Energy Mater. Sol. Cells*, vol. 127, pp. 50–57, 2014.

[5] Mckinsey, “Lighting the way: Perspectives on the global lighting market,” p. 68, 2012.

[6] R. H. Friend, R. W. Gymer, A. B. Holmes, J. H. Burroughes, R. N. Marks, C. Taliani, D. D. C. Bradley, D. A. Dos Santos, J. L. Bredas, M. Logdlund, and W. R. Salaneck, “Electroluminescence in conjugated polymers,” *Nature*, vol. 397, no. 6715, pp. 121–128, Jan. 1999.

[7] C.-C. Wu, J. C. Sturm, R. A. Register, J. Tian, E. P. Dana, and M. E. Tnompson, “Efficient organic electroluminescent devices using single-layer doped polymer thin films with bipolar carrier transport abilities,” *Electron Devices, IEEE Trans.*, vol. 44, no. 8, pp. 1269–1281, 1997.

[8] H. J. Lee, T. H. Park, J. H. Choi, E. H. Song, S. J. Shin, H. Kim, K. C. Choi, Y. W. Park, and B. K. Ju, “Negative mold transfer patterned conductive polymer electrode for flexible organic light-emitting diodes,” *Org. Electron. physics, Mater. Appl.*, vol. 14, no. 1, pp. 416–422, 2013.

[9] M. Singh, H. M. Haverinen, P. Dhagat, and G. E. Jabbour, “Inkjet printing-process and its applications,” *Adv. Mater.*, vol. 22, no. 6, pp. 673–685, 2010.

[10] “556696 @ www.sigmaaldrich.com.” (10.07.2015).

[11] D. R. Cairns, R. P. W. Ii, D. K. Sparacin, S. M. Sachsman, D. C. Paine, and G. P. Crawford, “on Polymer Substrates,” vol. 76, no. 11, pp. 1425–1427, 2000.

[12] L. Pauling, “The nature of the chemical bond. Application of results obtained from the quantum mechanics and from a theory of paramagnetic susceptibility to the structure of molecules,” *J. Am. Chem. Soc.*, vol. 53, no. 4, pp. 1367–1400, 1931.

[13] “organic-semiconductors @ oelectronics.weebly.com.” (06.05.2015).

[14] R. Trattnig, “Organic Light Emitting Devices based on Phosphorescent Organometallic Complexes in Blend- and Onchain Polymer Systems,” no. April, 2009.

[15] J. E. Huheey, E. a. Keiter, and R. L. Keiter, *Inorganic Chemistry: Principles of Structure and Reactivity (4th Edition)*. HarperCollins College Publishers, 1993.

[16] C. A. Coulson, *Valence*. Clarendon Press, 1953.

[17] G. L. Miessler, P. J. Fischer, and D. A. Tarr, *Inorganic Chemistry: Pearson New International Edition*. Pearson Higher Ed, 2013.

[18] A. D. McNaught and A. D. McNaught, *Compendium of chemical terminology*, vol. 1669. Blackwell Science Oxford, 1997.

[19] D. I. H. Scheiber, "Structure to Property Relationships in Blue Light Emitting Conjugated Polymers," no. June, 2008.

[20] R. Marcus, "On the Theory of Oxidation and Reduction Reactions Involving Electron Transfer," *J. Chem. Phys.*, vol. 42, no. 1952, pp. 966–978, 1956.

[21] H. Shirakawa, E. J. Louis, A. G. MacDiarmid, C. K. Chiang, and A. J. Heeger, "Synthesis of electrically conducting organic polymers: halogen derivatives of polyacetylene, (CH)," *J. Chem. Soc. Chem. Commun.*, no. 16, pp. 578–580, 1977.

[22] L. D. Landau and S. I. Pekar, "Effective Mass of a Polaron," *Sci. York*, vol. 423, no. 5, pp. 71–74, 1948.

[23] S. Roth and D. Carroll, *One-Dimensional Metals: Conjugated Polymers, Organic Crystals, Carbon Nanotubes*. Wiley, 2006.

[24] H. Ibach and H. Lüth, *Solid-state physics: An introduction to principles of materials science*, vol. 144, no. 3624. 2010.

[25] H. Yersin and K. L. Bray, *Transition Metal and Rare Earth Compounds III: Excited States, Transitions, Interactions*. Springer, 2004.

[26] M. Born and R. Oppenheimer, "Zur quantentheorie der molekeln," *Ann. Phys.*, vol. 20, no. 84, pp. 457–484, 1927.

[27] M. H. M. Pienn and Michael H. M. Pienn, "Application of Blue-Emitting Ladder- Type Poly(para-phenylene)s for Solid State Lighting: Efficiency Improvement and Colour Tuning," no. November 2008, 2008.

[28] H. Haken and H. C. Wolf, "Molekülphysik und Quantenchemie: Einführung in die experimentellen und theoretischen Grundlagen," *Springer-Verlag, Berlin Heidelb.*, pp. 153–296, 2006.

[29] E. U. Condon, "Nuclear motions associated with electron transitions in diatomic molecules," *Phys. Rev.*, vol. 32, no. 6, pp. 858–872, 1928.

[30] E. Condon, "A theory of intensity distribution in band systems," *Phys. Rev.*, vol. 28, no. 6, pp. 1182–1201, 1926.

[31] J. Franck, "Elementary processes," no. 1923, pp. 536–542, 1924.

[32] M. Pope and C. E. Swenberg, *Electronic Processes in Organic Crystals and Polymers*. Oxford University Press, 1999.

[33] a. Jabłoński, “Efficiency of Anti-Stokes Fluorescence in Dyes,” *Nature*, vol. 131, no. 3319, pp. 839–840, 1933.

[34] W. Schnabel, *Polymers and Light: Fundamentals and Technical Applications*. 2007.

[35] S. Braun, W. R. Salaneck, and M. Fahlman, “Energy-level alignment at organic/metal and organic/organic interfaces,” *Adv. Mater.*, vol. 21, no. 14–15, pp. 1450–1472, 2009.

[36] N. Koch, “Organic electronic devices and their functional interfaces,” *ChemPhysChem*, vol. 8, no. 10, pp. 1438–1455, 2007.

[37] H. Ishii, K. Sugiyama, E. Ito, and K. Seki, “Energy level alignment and interfacial electronic structures at organic/metal and organic/organic interfaces,” *Adv. Mater.*, vol. 11, no. 8, pp. 605 – 625, 1999.

[38] S. Nau, N. Schulte, S. Winkler, J. Frisch, A. Vollmer, N. Koch, S. Sax, and E. J. W. List, “Highly efficient color-stable deep-blue multilayer PLEDs: Preventing PEDOT:PSS-induced interface degradation,” *Adv. Mater.*, vol. 25, no. 32, pp. 4420–4424, 2013.

[39] T. R. Society, R. Society, C. Papers, and P. Character, “Electron Emission in Intense Electric Fields Author (s): R . H . Fowler and L . Nordheim Source : Proceedings of the Royal Society of London . Series A , Containing Papers of a Published by : The Royal Society Stable URL : http://www.jstor.org/stable/95,” vol. 119, no. 781, pp. 173–181, 2010.

[40] J. C. Scott and G. G. Malliaras, “Charge injection and recombination at the metal–organic interface,” *Chem. Phys. Lett.*, vol. 299, no. 2, pp. 115–119, 1999.

[41] C. W. Tang and S. a. Vanslyke, “Organic electroluminescent diodes,” Appl. Phys. Lett., vol. 51, no. 1987, pp. 913–915, 1987.

[42] “Aluminium-tris(8-hydroxychinolin) @ de.wikipedia.org.” (08.05.2015).

[43] “Poly-3,4-ethylendioxythiophen @ de.wikipedia.org.” (14.07.2015).

[44] M. Thesis, “Efficiency and Stability of Poly (indenofluorene) -based Homo- and Copolymers,” no. April, 2011.

[45] “Indiumzinnoxid @ de.wikipedia.org.” (23.09.2015).

[46] G. Hautier, A. Miglio, G. Ceder, G.-M. Rignanese, and X. Gonze, “Identification and design principles of low hole effective mass p-type transparent conducting oxides.,” *Nat. Commun.*, vol. 4, p. 2292, 2013.

[47] G. Horowitz, P. Delannoy, and H. Bouchriha, “Two-layer light-emitting diodes based on sexithiophene and derivatives,” *Advanced*, pp. 752–755, 1994.

[48] “indium @ www.technologiemetalle.org.” (01.10.2015).

[49] S. Harkema, S. Mennema, M. Barink, H. Rooms, J. S. Wilson, T. van Mol, and D. Bollen, “Large area ITO-free flexible white OLEDs with Orgacon PEDOT:PSS and printed metal shunting lines,” *Proc. SPIE*, vol. 7415, no. 0, p. 74150T–74150T–8, 2009.

[50] J. Park, J. Lee, D. Shin, and S. Park, “Luminance uniformity of large-area OLEDs with an auxiliary metal electrode,” *IEEE/OSA J. Disp. Technol.*, vol. 5, no. 8, pp. 306–311, 2009.

[51] M.-G. Kang and L. J. Guo, “Nanoimprinted Semitransparent Metal Electrodes and Their Application in Organic Light-Emitting Diodes,” *Adv. Mater.*, vol. 19, no. 10, pp. 1391–1396, 2007.

[52] F. L. M. Sam, M. A. Razali, K. D. G. I. Jayawardena, C. A. Mills, L. J. Rozanski, M. J. Beliatis, and S. R. P. Silva, “Silver grid transparent conducting electrodes for organic light emitting diodes,” *Org. Electron.*, vol. 15, no. 12, pp. 3492–3500, Dec. 2014.

[53] D. Zhang, K. Ryu, X. Liu, E. Polikarpov, J. Ly, M. E. Tompson, and C. Zhou, “Transparent, Conductive, and Flexible Carbon Nanotube Films and Their Application in Organic Light-Emitting Diodes,” *Nano Lett.*, vol. 6, no. 9, pp. 1880–1886, Sep. 2006.

[54] J. Li, L. Hu, L. Wang, Y. Zhou, G. Grüner, and T. J. Marks, “Organic Light-Emitting Diodes Having Carbon Nanotube Anodes,” *Nano Lett.*, vol. 6, no. 11, pp. 2472–2477, Nov. 2006.

[55] M. W. Rowell, M. a. Topinka, M. D. McGehee, H.-J. Prall, G. Dennler, N. S. Sariciftci, L. Hu, and G. Gruner, “Organic solar cells with carbon nanotube network electrodes,” *Appl. Phys. Lett.*, vol. 88, no. 23, p. 233506, 2006.

[56] L. Hu, D. S. Hecht, and G. Grüner, “Percolation in Transparent and Conducting Carbon Nanotube Networks,” *Nano Lett.*, vol. 4, no. 12, pp. 2513–2517, Dec. 2004.

[57] A. Kumar and C. Zhou, “The race to replace tin-doped indium oxide: Which material will win?,” *ACS Nano*, vol. 4, no. 1, pp. 11–14, 2010.

[58] S. De, T. M. Higgins, P. E. Lyons, E. M. Doherty, P. N. Nirmalraj, W. J. Blau, J. J. Boland, and J. N. Coleman, “Silver Nanowire Networks as Flexible ,” *ACSNano*, vol. 3, no. 7, pp. 1767–1774, 2009.

[59] J. Park and H. Ham, “Sputter-patterned ITO-based organic light-emitting diodes with leakage current cut-off layers,” *Org. Electron. physics, Mater. Appl.*, vol. 12, no. 11, pp. 1872–1878, 2011.

[60] Y. S. Kim, M. H. Chang, E. J. Lee, D. W. Ihm, and J. Y. Kim, “Improved electrical conductivity of PEDOT-based electrode films hybridized with silver nanowires,” *Synth. Met.*, vol. 195, pp. 69–74, 2014.

[61] J. Y. Lee, S. T. Connor, Y. Cui, and P. Peumans, “Solution-processed metal nanowire mesh transparent electrodes,” *Nano Lett.*, vol. 8, pp. 689–692, 2008.

[62] W. Gaynor, G. F. Burkhard, M. D. McGehee, and P. Peumans, “Smooth nanowire/polymer composite transparent electrodes,” *Adv. Mater.*, vol. 23, pp. 2905–2910, 2011.

[63] a K. Geim and K. S. Novoselov, “The rise of graphene,” *Nat. Mater.*, vol. 6, no. 3, pp. 183–191, 2007.

[64] T. Fang, A. Konar, H. Xing, and D. Jena, “Carrier statistics and quantum capacitance of graphene sheets and ribbons,” *Appl. Phys. Lett.*, vol. 91, no. 2007, p. 092109, 2007.

[65] J. Wu, M. Agrawal, H. A. Becerril, Z. Bao, Z. Liu, Y. Chen, and P. Peumans, “Organic Light-Emitting Diodes on Solution-Processed Graphene Transparent Electrodes,” *ACS Nano*, vol. 4, no. 1, pp. 43–48, Jan. 2010.

[66] “Inkjet_printing @ en.wikipedia.org.” (25.08.2015).

[67] S. Magdassi, “Ink requirements and formulations guidelines,” in *The chemistry of inkjet inks*, Singapore: World Scientific Publishing, 2010, pp. 19–41.

[68] H. J. Gysling, “Nanoinks in inkjet metallization - Evolution of simple additive-type metal patterning,” *Curr. Opin. Colloid Interface Sci.*, vol. 19, no. 2, pp. 155–162, 2014.

[69] “http://www.microdrop.de.” (13.07.2015).

[70] T. Effect, K. D. Sites, E. Properties, and P. Materials, “The Effect of Keto Defect Sites on the Emission Properties of Polyfluorene-Type Materials**,” no. 5, pp. 374–378, 2002.

[71] H. C. L. O. Miesbauer, M. Schmidt, *Vakuum in Forschung und Praxis*. 2008.

[72] S. Kappaun, H. Scheiber, R. Trattnig, E. Zojer, E. J. W. List, and C. Slugovc, “Defect chemistry of polyfluorenes: identification of the origin of {.”

[73] M. Schaer, F. Nüesch, D. Berner, W. Leo, and L. Zuppiroli, “Water vapor and oxygen degradation mechanisms in organic light emitting diodes,” *Adv. Funct. Mater.*, vol. 11, no. 2, pp. 116–121, 2001.

[74] G. Greczynski, T. Kugler, M. Keil, W. Osikowicz, M. Fahlman, and W. R. Salaneck, “Photoelectron spectroscopy of thin films of PEDOT-PSS conjugated polymer blend: A mini-review and some new results,” *J. Electron Spectros. Relat. Phenomena*, vol. 121, no. 1–3, pp. 1–17, 2001.

[75] A. Van Dijken, A. Perro, E. A. Meulenkamp, and K. Brunner, “The influence of a PEDOT:PSS layer on the efficiency of a polymer light-emitting diode,” *Org. Electron. physics, Mater. Appl.*, vol. 4, no. 2–3, pp. 131–141, 2003.

[76] P. J. Brewer, J. Huang, P. A. Lane, A. J. deMello, D. D. C. Bradley, and J. C. deMello, “Influence of poly(3,4-ethylenedioxythiophene)-poly(styrenesulfonate) in polymer LEDs,” *Phys. Rev. B*, vol. 74, no. 11, p. 115202, Sep. 2006.

[77] P. J. Brewer, P. A. Lane, J. Huang, A. J. deMello, D. D. C. Bradley, and J. C. deMello, “Role of electron injection in polyfluorene-based light emitting diodes containing PEDOT:PSS,” *Phys. Rev. B*, vol. 71, no. 20, p. 205209, 2005.

[78] C. Y. Chang, F. Y. Tsai, S. J. Jhuo, and M. J. Chen, “Enhanced OLED performance upon photolithographic patterning by using an atomic-layer-deposited buffer layer,” *Org. Electron. physics, Mater. Appl.*, vol. 9, no. 5, pp. 667–672, 2008.

[79] J. Gruner, P. J. Hamer, R. H. Friend, H. Huber, U. Schera, and A. B. Holmes, “A High Efficiency Blue-Light-Emitting Diode Based on Novel Ladder Poly(p-phenylene)s,” *Adv. Mater.*, vol. 6, no. 10, pp. 748–752, 1994.

[80] G. Malliaras, J. Salem, P. Brock, and C. Scott, “Electrical characteristics and efficiency of single-layer organic light-emitting diodes,” *Phys. Rev. B*, vol. 58, no. 20, pp. R13411–R13414, 1998.

[81] F. Lu, X. Liu, and Y. Xing, “Numerical study of the influence of applied voltage on the current balance factor of single layer organic light-emitting diodes,” *J. Appl. Phys.*, vol. 115, no. 16, p. 164508, 2014.

[82] a. Doraiswamy, C. Jin, R. J. Narayan, P. Mageswaran, P. Mente, R. Modi, R. Auyeung, D. B. Chrisey, a. Ovsianikov, and B. Chichkov, “Two photon induced polymerization of organic-inorganic hybrid biomaterials for microstructured medical devices,” *Acta Biomater.*, vol. 2, no. 3, pp. 267–275, 2006.

[83] K.-B. Kim, Y.-H. Tak, Y.-S. Han, K.-H. Baik, M.-H. Yoon, and M.-H. Lee, “ Relationship between Surface Roughness of Indium Tin Oxide and Leakage Current of Organic Light-Emitting Diode ,” *Jpn. J. Appl. Phys.*, vol. 42, no. Part 2, No. 4B, pp. L438–L440, 2003.

[84] R. D. Deegan, O. Bakajin, T. F. Dupont, G. Huber, S. R. Nagel, and T. A. Witten, “Capillary flow as the cause of ring stains from dried liquid drops,” *Nature*, vol. 389, no. 6653, pp. 827–829, 1997.

11 List of figures